PNNL Phase 1 Update on Sibling Pin Destructive Examination Results

Spent Fuel and Waste Disposition

Prepared for
US Department of Energy
Spent Fuel and Waste Science and Technology

Pacific Northwest National Laboratory
RW Shimskey, JR Allred,
RC Daniel, MK Edwards, J Geeting,
PJ MacFarlan, LI Richmond,
TS Scott, and BD Hanson

September 27, 2019
SFWD-SFWST-M2SF-19PN010201037
PNNL-29179

SUMMARY

The Office of Spent Fuel and Waste Disposition within the U.S. Department of Energy Office of Nuclear Energy (DOE-NE) established the Spent Fuel and Waste Science and Technology campaign to conduct research and development activities related to storage, transportation, and disposal of spent nuclear fuel and high-level radioactive waste. DOE-NE, in partnership with the Electric Power Research Institute (EPRI), developed the High Burnup Spent Fuel Data Project to perform a large-scale demonstration and laboratory-scale testing of high burnup fuels (exceeding 45 gigawatt-days per metric ton of uranium [GWd/MTU]). Under this project, 25 sibling pins (aka sister rods)—i.e., rods having the same design, power histories, and other characteristics—were removed from assemblies at the North Anna Nuclear Power Station and sent to Oak Ridge National Laboratory (ORNL) in January 2016. ORNL performed detailed nondestructive examination (NDE) of all 25 rods. The NDE consisted of visual examinations, gamma and neutron scanning, profilometry and rod length measurements, and eddy current examinations. Upon completion of the NDE, 10 of the sibling pins were delivered to the Pacific Northwest National Laboratory (PNNL) in the NAC International, Inc. legal-weight truck cask in September 2018 for destructive examination. Each rod was individually drawn into the hot cell, where it was punctured to determine the end-of-life rod internal pressure, internal volume, and isotopic composition of the gas within the rod. This information was compared to estimated total quantities expected based on the specific rod design and utility-provided irradiation histories and discussion in Shimskey et al. 2019[a]. After gas puncture, each of the 10 received rods was cut into four segments and placed into storage in inerted storage tubes.

This report discusses PNNL's progress in preparation for Phase 1 testing as outlined in Saltzstein et al. 2018.[b] Preliminary gas communication testing performed on the bottom segment of rod 6U3L08 (segment UL-4, 36-in. length) was compared to the full-length results at ORNL for rod 30AK09, showing similar estimates for hydraulic diameter between 46 and 75 µm. Physical diameter changes of ~ 2 µm for segment UL-4 were measured during testing while pressurized to 5 MPa. These results are within the uncertainty of the optical micrometer and additional testing to determine actual uncertainties and reproducibility will be performed.

Gas communication testing also took steps to evaluate and quantify particle release during rod depressurization (i.e., during gas communication "decay" testing). Estimates of total release based on ^{134}Cs, ^{137}Cs, and ^{154}Eu activities in this sample yield total aerosol fractional release in the range of 10^{-8} to 10^{-7} kg fuel release per kg fuel in rod. In comparison, Hanson et al. (2008)[c] observed fractional releases ranging from 10^{-7} to 10^{-5} for much smaller segments of high burnup spent nuclear fuel (both pressurized water reactor and boiling water reactor samples). As such, the fraction released in the current testing seems in line with previous measurements of fuel release.

Dissolution of spent fuel from two spent fuel samples from rod 6U3L08 (sample UL-3-1, 5.98 in. length) and rod F35K13 (sample FK-4-1, 3.36-in. length) also occurred, demonstrating that dissolution from samples up to 6 in. length was achievable within a day of operation without drilling. Dose measurements of these defueled cladding samples confirmed that most destructive testing of the defueled cladding could occur outside the hot cell.

---

[a] Shimskey R.W., M.K. Edwards, J. Geeting, J.R. Allred, S.K. Cooley, R.C. Daniel, and R.M. Cox, et al. 2019. Initial Results of Destructive Examination of Ten Sister Rods at PNNL. PNNL-28548. Pacific Northwest National Laboratory, Richland, Washington.

[b] Saltzstein, S.J., M. Billone, B. Hanson, and J. Scaglione. 2018. *Visualization of the High-Burnup Spent Fuel Rod Phase 1 Test Plan: Technical Memo*. SAND2018-8042 O, Sandia National Laboratories, Albuquerque, New Mexico.

[c] Hanson, B.D., R.C. Daniel, A. Casella, R.S. Wittman, W. Wu, P.J. MacFarlan, and R.W. Shimskey. 2008. Fuel-In-Air FY07 Summary Report. PNNL-17275, Rev. 1, Pacific Northwest National Laboratory, Richland, Washington.

Development of the burst system for elevated temperature testing is on track as is the establishment of an optical metallurgical center for cross sectional imaging and microhardness measurements of defueled cladding. The LECO hydrogen analyzer has been operational for the last year and is currently running radiological samples in a ventilated enclosure.

ACKNOWLEDGEMENTS

The work reported here was performed at Pacific Northwest National Laboratory (PNNL) and supported by the U.S. Department of Energy Spent Fuel and Waste Science and Technology (SFWST) Storage and Transportation program, Office of Nuclear Energy (NE-81). The authors are thankful for the leadership of Ned Larson in NE-81 and to NE-81 staff Jorge Monroe-Rammsy.

We thank the SFWST Storage and Transportation control account leadership of Sylvia Saltzstein at Sandia National Laboratories. We also thank the reviewers at Sandia National Laboratories, Argonne National Laboratory, and Oak Ridge National Laboratory.

This work would not have been possible without the expertise of Randy Thornhill and his vast experience working with commercial spent nuclear fuel. The Shielded Facility Operations team of Franciska Steen, Jake Bohlke, Bob Orton, Jason Cartwright, Dustin Blundon, Jordon Condray, Jarrod Turner, and Jeff Chenault were invaluable, and their dedication and long hours are greatly appreciated.

We are thankful to the project support team of Alma Contreras, Lisa Middleton-Smith, and Chrissy Charron.

Lastly, we are thankful for Matt Wilburn’s expertise in editing and formatting this report.

This page is intentionally left blank.

CONTENTS

SUMMARY iii

ACKNOWLEDGEMENTS v

REVISION HISTORY xi

ACRONYMS xiii

1. INTRODUCTION 1
    - 1.1 Quality Assurance 1
2. GAS COMMUNICATION 3
    - 2.1 Test Apparatus 3
    - 2.2 Technical Basis 4
        - 2.2.1 Background 4
        - 2.2.2 PNNL Gas Communication Model 7
            - 2.2.2.1 Pressure Reservoir Dynamics 8
            - 2.2.2.2 Gas Flow Dynamics 9
            - 2.2.2.3 Gas Communication Pressure Dynamics 11
    - 2.3 Results 13
        - 2.3.1 Analysis of ORNL Data for Rod 30AK09 14
        - 2.3.2 Analysis of PNNL Data for Rod Segment UL-4 16
    - 2.4 Secondary Data 20
        - 2.4.1 Rod Diameter Measurements 20
        - 2.4.2 Particle Release Measurements 20
    - 2.5 Summary 23
3. FUEL DISSOLUTION 25
    - 3.1 Dissolution Apparatus 25
    - 3.2 Test Dissolution 30
        - 3.2.1 Results 33
        - 3.2.2 ICP-MS Results 35
        - 3.2.3 Smear Gamma Energy Analysis (GEA) Results 35
        - 3.2.4 Dose Measurements 37
4. BURST SYSTEM 41
    - 4.1 Burst System Apparatus 41
5. METALLURGICAL TESTING 45
    - 5.1 Metallography Sample Preparation and Examination 45
        - 5.1.1 Sample Preparation 45
    - 5.2 LECO Measurement of Hydrogen, Oxygen, and Nitrogen in Cladding Samples 49
        - 5.2.1 Instrument Modifications 50
        - 5.2.2 Sample Preparation 51
6. SUMMARY 53
7. REFERENCES 55

APPENDIX A: GAS COMMUNICATION MODEL DEVELOPMENT A-1

This page is intentionally left blank.

LIST OF FIGURES

Figure 1-1. Phase 1 Test Plan Visualization (Saltzstein et al. 2018) 2

Figure 2-1. Gas Communication Testing Apparatus.......... 4

Figure 2-2. Conceptual Simplified Model Used by Coulson and Richardson (1997) for Compressible Gas Transmission.......... 5

Figure 2-3. ORNL Pressurization Data for Rod 30AK09 Taken from Montgomery and Morris 2019, Figure 8. 15

Figure 2-4. PNNL Pressure Balance Data for Rod Segment UL-4. 18

Figure 2-5. PNNL Pressure Decay Data for Rod Segment UL-4. 19

Figure 2-6. To-scale Drawing of the Volume Downstream of the Rod. 22

Figure 3-1. Simplified Dissolution System P&ID 27

Figure 3-2. Photos of Dissolution System: (top) Front View and (bottom) Side View 28

Figure 3-3. Dissolution Basket. 29

Figure 3-4. Rinse Basket and Rinse Cylinder 29

Figure 3-5. Batch Dissolution Flowsheet 30

Figure 3-6. Test Dissolution System 31

Figure 3-7. Test Dissolution of Sample FK-4-1 32

Figure 3-8. De-fueled Sample UL-3-1 33

Figure 3-9. Leached and Cleaned Sample UL-3-1 33

Figure 3-10. Dose Measurement Location Diagram 37

Figure 4-1. Burst System Schematic 43

Figure 4-2. Equipment Located on Movable Table 43

Figure 4-3. Custom Oven Before and After Insulating 44

Figure 5-1. Isomet Low-Speed Saw 46

Figure 5-2. Vibratory Polisher and Multistage Polisher 46

Figure 5-3. Optical Image of Mounted and Polished Non-Irradiated, Pre-hydrided Cladding 47

Figure 5-4. Olympus Optical Microscope 48

Figure 5-5. Microhardness Tester 48

Figure 5-6. Optical Image of Microhardness Indentations 49

Figure 5-7. a) As Manufactured LECO ONH 836 instrument, b) LECO ONH 836 Fit into Fumehood 90°, c) LECO ONH 836 with Reagent Covers Removed, d) Arm Holes Cut in the Side of the Fumehood 50

LIST OF TABLES

Table 2-1. Description Gas Communication Rod Samples Analyzed 14

Table 2-2. Analysis of Time Constants Derived from Figure 2-3 Analysis from ORNL Rod 30AK09 Pressurizations Test Data Reported in Montgomery and Morris 2019. 15

Table 2-3. Tabulated Results of Analysis of Balance and Decay Pressure Testing of PNNL Rod Segment UL-4. 17

Table 2-4. Laser micrometer rod diameters measured for rod blanks and Rod Segment UL-4. 20

Table 2-5. GEA Counting Results for Fuel Release during Depressurization of Rod Segment UL-4. 21

Table 3-1. Dissolution Testing Sample Description 25

Table 3-2. Dissolution Conditions 31

Table 3-3. Sample UL-3-1 Depth Gauge Checks 34

Table 3-4. Sample FK-4-1 Depth Gauge Checks 34

Table 3-5. Test Dissolution Samples (post-dissolution, before leach) 34

Table 3-6. Mass Removal from Cleaning Process 34

Table 3-7. Rare Earth and Actinide ICP-MS Results 35

Table 3-8. Uranium Enrichment ICP-MS Results 35

Table 3-9. Sample UL-3-1 Smear GEA Results 36

Table 3-10. Sample FK-4-1 Smear GEA Results 36

Table 3-11. Blank Smear GEA Results 37

Table 3-12. Measured Dose Rates for Sample UL-3-1 38

Table 3-13. Measured Dose Rates for Sample FK-4-1 38

Table 3-14. Decontamination Factors for Sample UL-3-1 39

Table 3-15. Decontamination Factors for Sample FK-4-1 39

REVISION HISTORY

REVISION	COMMENTS	ISSUE DATE
Draft	Initial release for programmatic review	August 27, 2019
0	Address comments from programmatic review. Initial public release.	September 27, 2019

This page is intentionally left blank.

ACRONYMS

DE	destructive examination
DF	decontamination factor
DOE	U.S. Department of Energy
EPRI	Electric Power Research Institute
GEA	gamma energy analysis
GWd	gigawatt-day
HBU	high burnup
HLRF	High-Level Radiochemistry Facility
ICP-MS	inductively coupled plasma mass spectrometry
IR	infrared
LECO	The LECO Corporation
MTU	metric tons of uranium
NDE	nondestructive examination
NDIR	non-dispersive infrared
NE	Office of Nuclear Energy
NIST	National Institute of Standards and Technology
ODE	ordinary differential equation
ORNL	Oak Ridge National Laboratory
PID	proportional, integral, derivative
PNNL	Pacific Northwest National Laboratory
psia	pounds per square inch absolute
SFWST	Spent Fuel and Waste Science and Technology
SNF	spent nuclear fuel
SST	stainless steel
TC	thermal conductivity
WDH	width, depth, height

TRADEMARKS

Airmo®	Airmo is a trademark and brand of Airmo, Inc. in the United States and in other countries.
M5®	Registered trademark of Framatome (formerly AREVA NP) registered in the United States and in other countries
ZIRLO®	Registered trademark of Westinghouse Electric Company LLC in the United States and in other countries

PNNL PHASE 1 UPDATE ON SIBLING PIN DESTRUCTIVE EXAMINATION RESULTS

1. INTRODUCTION

The Office of Spent Fuel and Waste Disposition within the U.S. Department of Energy Office of Nuclear Energy (DOE-NE) established the Spent Fuel and Waste Science and Technology (SFWST) campaign to conduct research and development activities related to storage, transportation, and disposal of spent nuclear fuel (SNF) and high-level radioactive waste. The initial emphasis of the program is on uranium-oxide fuel from commercial light-water reactors. Because limited information is available about the properties of high burnup (HBU) fuel (exceeding 45 gigawatt-days per metric ton of uranium [GWd/MTU]) and because much of the fuel currently discharged from commercial reactors exceeds this burnup threshold, this program is particularly focused on HBU fuels.

DOE-NE, in partnership with the Electric Power Research Institute (EPRI), developed the High Burnup Spent Fuel Data Project to perform a large-scale demonstration and laboratory-scale testing of HBU fuels (EPRI 2014). Under this project, a storage cask (TransNuclear TN-32B) licensed by the U.S. Nuclear Regulatory Commission was loaded in November 2017 with 32 HBU assemblies from the pressurized water reactors at Dominion’s North Anna Nuclear Power Station in Mineral, Virginia. Prior to loading the Research Project Cask, 25 HBU fuel rods, referred to as sibling pins (aka sister rods) because they have the same design and similar characteristics (e.g., power histories), were removed from assemblies and sent to Oak Ridge National Laboratory (ORNL) in January 2016. ORNL performed detailed nondestructive examination (NDE) of all 25 rods (Montgomery et al. 2018). The NDE consisted of visual examinations, gamma and neutron scanning, profilometry and rod length measurements, and eddy current examinations. Upon completion of the NDE, 10 of the sibling pins were sent to Pacific Northwest National Laboratory (PNNL) in September 2018 for destructive examination (DE). Phase 1 of the DE testing at PNNL and ORNL is described in the test plan visualization in Figure 1-1 (Saltzstein et al. 2018).

PNNL has completed gas puncture testing, gas analysis, and sectioning of the 10 received sibling pins as discussed in Shimskey et al. 2019. This report documents PNNL’s progress in support of Phase 1 testing since then. Section 2 discusses the status of gas communication testing of sectioned rods and analysis of initial results. Section 3 discusses the methodology of dissolving fuel from samples of the sibling pins and initial dissolution results of two fuel rod samples. Section 4 discusses the development of the burst system and equipment involved. Section 5 discusses the equipment and methods used to characterize the hydrogen orientation and concentration in the rods as well as measure microhardness. Finally, Section 6 summarizes the progress of these activities.

1.1 Quality Assurance

This work has been assigned a Quality Rigor Level 3 by SFWST. As such, the work is done in accordance with the PNNL laboratory-wide Quality Assurance Program that is compliant with DOE Order 414.1 and a graded approach based on the American Society of Mechanical Engineers Nuclear Quality Assurance Standard, NQA-1-2000, Part I, Part II (Subpart 2.7) and Part IV (Subpart 4.2). Program procedures are written to follow ASTM International consensus standards, as applicable, with modifications made to account for safety and working with radioactive samples. Measuring and Test Equipment (e.g., balances, pressure transducers, thermocouples, standard volumes, data acquisition systems, etc.) for quality-affecting data are calibrated by a qualified supplier with standards traceable to the National Institute of Standards and Technology (NIST). Other systems (e.g., optical microscope, scanning electron microscope, optical micrometers, etc.) use NIST-traceable standards to verify system outputs. Data and project reports are reviewed by an Independent Technical Reviewer.

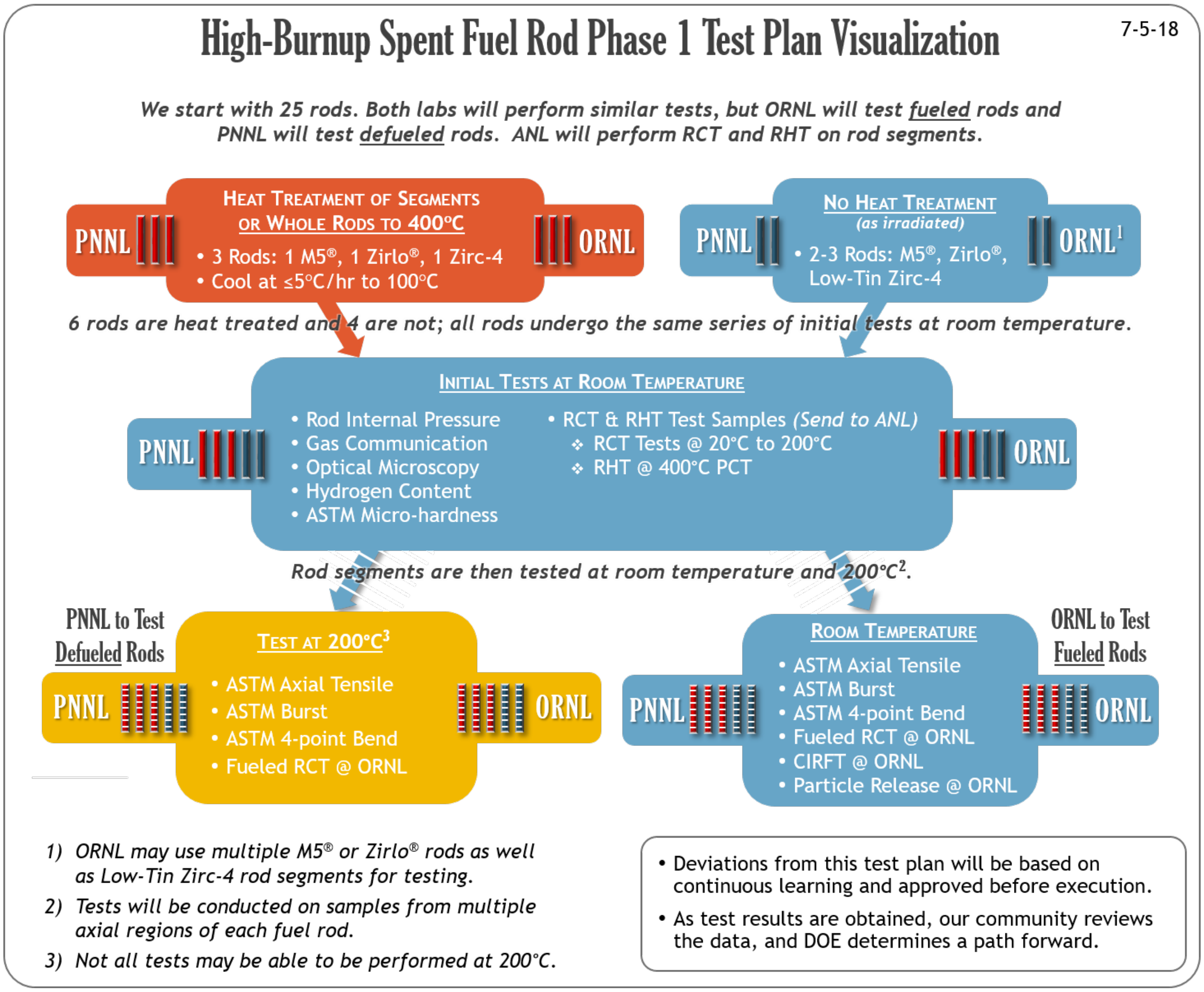

High-Burnup Spent Fuel Rod Phase 1 Test Plan Visualization

7-5-18

We start with 25 rods. Both labs will perform similar tests, but ORNL will test fueled rods and PNNL will test defueled rods. ANL will perform RCT and RHT on rod segments.

HEAT TREATMENT OF SEGMENTS OR WHOLE RODS TO 400°C

- 3 Rods: 1 M5®, 1 Zirlo®, 1 Zirc-4
- Cool at ≤5°C/hr to 100°C

NO HEAT TREATMENT
(as irradiated)

- 2-3 Rods: M5®, Zirlo®, Low-Tin Zirc-4

6 rods are heat treated and 4 are not; all rods undergo the same series of initial tests at room temperature.

INITIAL TESTS AT ROOM TEMPERATURE

- Rod Internal Pressure
- Gas Communication
- Optical Microscopy
- Hydrogen Content
- ASTM Micro-hardness
- RCT & RHT Test Samples *(Send to ANL)*
  - RCT Tests @ 20°C to 200°C
  - RHT @ 400°C PCT

Rod segments are then tested at room temperature and 200°C[2].

PNNL to Test Defueled Rods

TEST AT 200°C[3]

- ASTM Axial Tensile
- ASTM Burst
- ASTM 4-point Bend
- Fueled RCT @ ORNL

ORNL to Test Fueled Rods

ROOM TEMPERATURE

- ASTM Axial Tensile
- ASTM Burst
- ASTM 4-point Bend
- Fueled RCT @ ORNL
- CIRFT @ ORNL
- Particle Release @ ORNL

1) *ORNL may use multiple M5® or Zirlo® rods as well as Low-Tin Zirc-4 rod segments for testing.*
2) *Tests will be conducted on samples from multiple axial regions of each fuel rod.*
3) *Not all tests may be able to be performed at 200°C.*

- Deviations from this test plan will be based on continuous learning and approved before execution.
- As test results are obtained, our community reviews the data, and DOE determines a path forward.

Figure 1-1. Phase 1 Test Plan Visualization (Saltzstein et al. 2018)

2. GAS COMMUNICATION

Gas communication testing of the sibling pins involves evaluating the rate of gas transmission through the axial length of the spent fuel rods to provide 1) a rough measure of the time scale and gas flow rates associated with rod depressurization under accidental breach scenarios and 2) information regarding the internal microstructure of the SNF. Communication testing functions by exposing a 3- to 4-ft sub-segment of a sibling pin to either a high- or low-pressure reservoir and monitoring the time rate change in upstream / downstream pressure reservoirs with time. In general, the pressure reservoir volumes selected for testing are much larger than is prototypic of plenum or interstitial SNF rod volumes to facilitate measurable changes in pressure across easily resolvable time scales (minutes to hours) and to render the underlying physics amenable to analysis by analytic functions. As a result, the time-scales measured for gas transmission in gas communication do not necessarily correlate directly to those expected in actual accident release scenarios; rather, the results must be interpreted through first principles analysis to derive metrics by which transmission rates under prototypic storage and release conditions can be evaluated for scaling and to support safety basis analyses.

This section describes the experimental and analytical methods used to quantify the gas transmission properties of the sibling pins. Section 2.1 describes the gas communication test apparatus, test conduct of operations, and test fuel segment requirements. Section 2.2 presents the technical basis and first-principles equations for analyzing gas communication upstream and downstream gas reservoir pressure. Section 2.3 presents gas communication testing results for rod 30AK09 (tested by ORNL)[d] and PNNL rod segment UL-4 [the cut bottom segment from SNF rod 6U3L08 (Shimskey et al. 2019)]. Section 2.4 provides secondary data derived from gas communication testing, namely measurements of the rod segment UL-4 during pressurization and quantification of fuel release from the rod to downstream segments during depressurization of UL-4. Finally, Section 2.5 provides a summary and discussion of key findings from gas communication testing.

2.1 Test Apparatus

The communication device consists of two communication chambers (PCV1 and PCV2) on a moveable track so they may be securely placed using Airmo® grippers on opposite ends of a sibling pin segment. PCV1 is connected to an isolation valve (SIS-V-11) that is attached to the gas manifold in the back of the hot cells by a high-pressure gas line. PCV2 is connected to an isolation valve (SIS-V-13) before venting through a filter into the hot cell. Each communication chamber has a three-way valve to allow measurements in two pressure ranges [1) a larger range from atmospheric to 2500 psia and 2) a smaller range from atmospheric to 1015 psia] and thermocouples to measure chamber temperatures. Fixed on the communication device track are two optical micrometers at approximately 1/3 and 2/3 the length of the sibling pin segment, enabling the measurement of pin growth during pressurization. Utilizing helium gas, the gas manifold delivers test pressures via the high-pressure gas line to the communication chambers. The manifold further adds the capability of changing upstream volumes. A diagram of the testing apparatus can be seen in Figure 2-1.

---

[d] The basis for analyzing ORNL data for Rod 30AK09 is provided in Section 2.3.1.

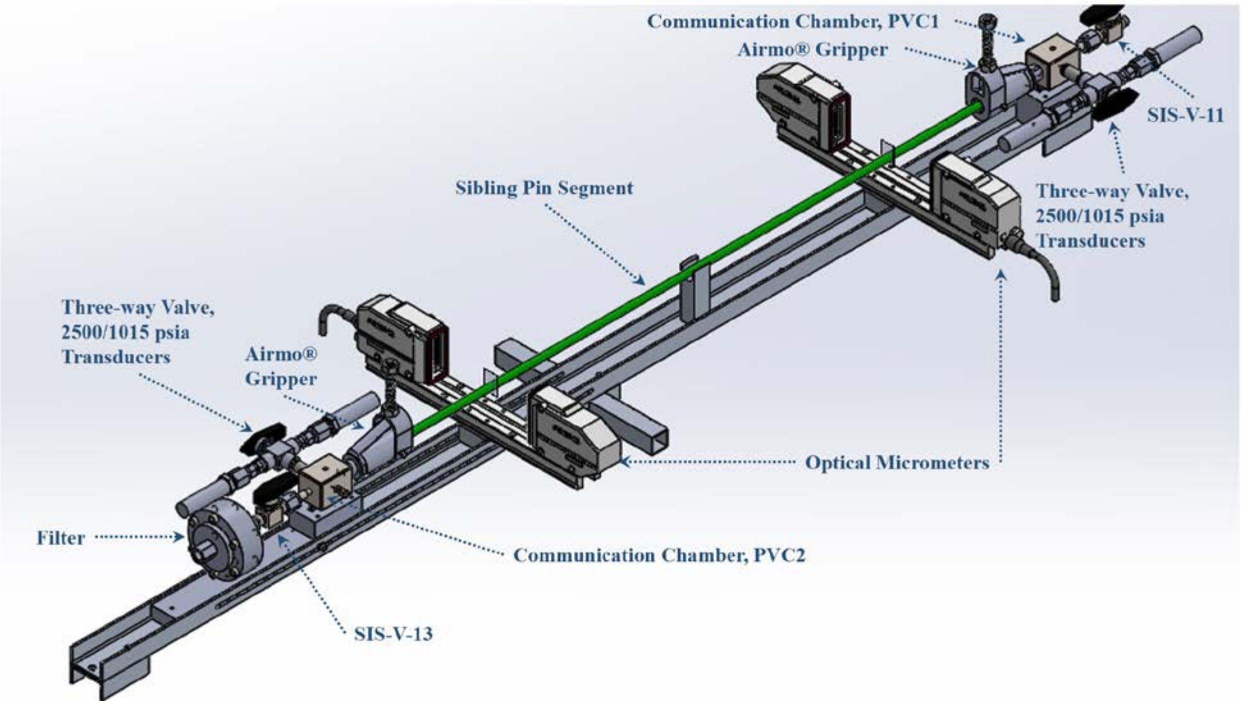

Figure 2-1. Gas Communication Testing Apparatus

2.2 Technical Basis

In this section, the technical basis for analyzing gas flow dynamics is developed. First, the basic equations for steady-state gas flow through pipes and structured media are presented. Then, these equations are used as a basis for developing, with some limiting assumptions, equations to interpret the microchannel media properties that control the rate of gas communication in SNF. It should be stated that the ultimate goal of analysis is to evaluate the time-scale for pressure equilibration within SNF rods during gas transmission events, rod permeability with respect to gas flow, and an equivalent hydrodynamic diameter that characterizes flow.

2.2.1 Background

Methods for analyzing transmission of compressible fluids through pipelines and porous media can be found in standard engineering handbooks (e.g., Coulson and Richardson 1997; Green 1997). The conceptual model for pipeline gas transmission provided by Coulson and Richardson (1997), shown in Figure 2-2, consists of a microchannel (pipe) bounded by two gas reservoirs: 1) an upstream (high-pressure) reservoir and 2) a downstream (low-pressure) reservoir. Transmission of gas through the pipeline is controlled by the thermodynamic conditions (i.e., pressure P, temperature T, and specific volume v[e]) of the upstream/downstream boundaries. In Coulson and Richardson's (1997) treatment of gas flow dynamics, several enabling assumptions are made:

- The gas is ideal such that temperature, pressure, and specific volume are related by:

  $$Pv = R_m T \qquad \text{Eq. (2.1)}$$

  where R_m is the individual constant of the gas.

---

[e] Specific volume v expresses the volume of gas per unit mass and has SI units of either m^3 mol^{-1} or m^3 kg^{-1}. As used in Eq.(2.1), where it is coupled with the individual gas constant R_m, the gas specific volume v has units of m^3 kg^{-1}.

- Both upstream conditions and downstream conditions are static (i.e., time independent).
- Flow is characterized by a steady mass flow rate G.
- The pipe is horizontal, such that the effects of gravity can be neglected.
- The microchannel / pipe is a straight conduit of length L and constant hydraulic diameter D.

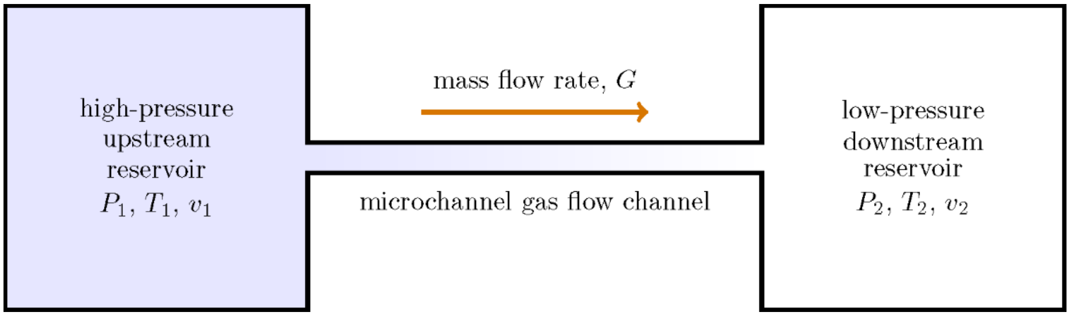

Figure 2-2. Conceptual Simplified Model Used by Coulson and Richardson (1997) for Compressible Gas Transmission.

Figure Note: Upstream and downstream conditions, denoted by the subscripts "1" and "2", respectively, are static. The mass flow rate through the channel is at pseudo-steady-state. Listed thermodynamic properties may not be independent.

These assumptions allow development of expressions that relate the mass flow rate G to the upstream and downstream conditions under isothermal and adiabatic thermodynamic regimes and develop corresponding conditions for choked mass flow. For isothermal flow, gas flow at a uniform temperature T_o, the equation that relates mass flow to the bounding conditions is:

$$\hat{\alpha}\left(\frac{G}{A}\right)^2 \ln\left(\frac{P_1}{P_2}\right)^2 + \frac{P_2^2 - P_1^2}{R_m T_o} + \frac{4 f_f L}{D}\left(\frac{G}{A}\right)^2 = 0 \qquad \text{Eq. (2.2)}$$

where A is the cross-sectional flow area and f_f is the Fanning friction factor. Equation (2.2) is general and holds under both laminar or turbulent flow (with $\hat{\alpha} = 1$ for turbulent flow, and $\hat{\alpha} = 2$ for laminar flow). For adiabatic gas flow, a similar expression results:

$$\hat{\alpha}\left(\frac{\gamma+1}{2\gamma}\right) \ln\left(\frac{v_1}{v_2}\right)^2 + \left[\frac{\gamma-1}{2\gamma} + \frac{P_1}{v_1}\left(\frac{A}{G}\right)^2\right]\left[1 - \left(\frac{v_1}{v_2}\right)^2\right] - \frac{4 f_f L}{D} = 0 \qquad \text{Eq. (2.3)}$$

where γ is the heat capacity ratio. As the upstream and downstream gas temperatures will not be equal under adiabatic flow conditions, solution of gas flow dynamics under adiabatic conditions requires simultaneous solution of Eq. (2.3) with:

$$\left(\frac{G}{A}\right)^2 v_1^2 + \left(\frac{2\gamma}{\gamma-1}\right) P_1 v_1 = \left(\frac{G}{A}\right)^2 v_2^2 + \left(\frac{2\gamma}{\gamma-1}\right) P_2 v_2 \qquad \text{Eq. (2.4)}$$

A key difference between the isothermal and adiabatic equations is that the latter is implicit in pressure difference. This means that one must first solve for the specific volume ratio v_1/v_2 and then solve for the corresponding pressure ratio P_2/P_1. This complicates analyses where the downstream temperature and specific volume may be unknown. Equations (2.2) and (2.3) can be used to derive critical flow conditions, namely the pressure (or alternatively, the specific volume ratio) at which maximal (choked) flow occurs. The maximum superficial gas velocity u_m for communication found through choked flow analysis is:

$$u_m = \sqrt{k P_w v_w} \qquad \text{Eq. (2.5)}$$

where k is a constant that ranges from 1 (for isothermal flow) to γ (for adiabatic flow) and P_w and v_w are the critical discharge pressure and specific volume, respectively. The latter two quantities do not generally equal the downstream pressure and specific volume; rather, they are the pressure and specific volume that maximize the mass flow rate G in Eqs. (2.2) and (2.3).

A key feature of gas flow, as quoted directly from Coulson and Richardson (1997), is:

> "The rate of flow gas under adiabatic conditions is never more than 20 percent greater than that obtained for the same pressure difference with isothermal conditions. For pipes of length at least 1000 diameters, the difference does not exceed about 5 per cent."

This suggests that, for a first-order treatment and analysis of gas flow conditions, the isothermal equation can be used without significant loss of accuracy even under cases where adiabatic conditions may hold. This is advantageous in that a single expression that can be solved directly with a given pipe pressure differential alone, which is typically known.

With respect to the current application involving analysis of gas transmission through the internal microstructure of SNF, the position that the microchannel is well-represented by a straight conduit of uniform diameter is untenable. The engineering literature offers means of addressing evaluating flow of gases through structured media. Here, the generalized expression for isothermal compressible flow in structured media (Green 1997) is:

$$G^2 \ln\left(\frac{P_1}{P_2}\right)^2 + \frac{P_2^2 - P_1^2}{R_m T} + \frac{4 f_m L (1-\epsilon)^{3-n}}{s^{3-n} \epsilon^3 d_p} G^2 = 0 \qquad \text{Eq. (2.6)}$$

where f_m is a modified friction factor, s and d_p are the surface-area-based shape factor and average particle diameter, respectively, of the particles that make up the structured medium, ϵ is the void fraction of the structured medium, and n is a performance factor that depends on a particle Reynolds number [see Fig 6-46 in Perry and Green (1997)] given by:

$$\mathrm{Re}_p = \frac{G d_p}{\mu} \qquad \text{Eq. (2.7)}$$

Here, μ represents the dynamic viscosity of the gas. Comparison of Eq. (2.6) to Eq. (2.2) suggests similar pressure and mass flow functionality. And there is indeed similar functionality under limiting conditions, as is evidenced by the fact that more limiting expressions for porous media flow (namely Darcy's Law) and capillary flow (Poiseuille's Law) also show analogous behavior [although the two describe flow through different media and cannot be equated rigorously (Dallavalle 1948)].

Is it important to note that, for the current analysis, the internal morphology of the SNF is not well-structured; rather, it is highly anisotropic with void spaces largely limited to a few irregular cracks and gaps between fuel pellets (Hanson et al. 2008). As such, Eq. (2.6), even when coupled with accurate estimates for void fraction and particle diameter and shape, may not provide a definitive means of relating flow and boundary conditions. And as noted before, the description of SNF flow channels (irregular cracks and inter-pellet spacings) with a single capillary model [Eq. (2.2)] appears similarly flawed.

There is no rigorous means of resolving the difficulties outlined above without resorting to numerical solutions derived from coupling of detailed models of internal SNF microstructure with sophisticated computational fluid dynamics solution schemes. To avoid the need to implement such models in the current report, analysis of gas flow dynamics herein will rely on the fact that flow in structured media can often been approximated with straight channel flow equations [cf. Darcy's law and use of single capillary expressions for examining liquid wicking behavior in porous media (Daniel and Berg 2006)]. In the current report, this means implementing Eq. (2.2) without regard to the actual structure of the SNF medium, and the primary impact of this approximation is the loss of physical significance the hydrodynamic parameters derived from fitting Eq. (2.2) to measured gas communication flow rates, assuming Eq. (2.2) even provides an adequate description of the observed flow dynamics.[f] Indeed, treatment of complex media with simplified flow channels generally yields apparent hydrodynamic lengths (such as a wicking equivalent diameter for imbibition of liquids into porous media) that are generally smaller than physical diameters/lengths of the individual channels within the complex medium.

Additional difficulties in treating SNF gas communication arise from the fact that, as implemented here and in previous SNF gas communication studies (Montgomery and Morris 2019), pressure in one or both of the upstream and downstream gas reservoirs varies until both reservoirs are at equal pressure. This means that the dynamics of one or both of the pressure reservoirs need to be coupled with the mass flow through the rod. Furthermore, as the upstream and downstream boundary conditions of the rod can change throughout the test, gas flow within the rod is also dynamic and never truly reaches the steady-state condition assumed in the derivation of Eqs. (2.2) and (2.3). In practice, this limitation can be overcome so long as the experimental setup guarantees that the time-scale associated with flow transients in the SNF rod are much smaller than those associated with upstream and downstream pressure transients. The latter would be accomplished by targeting upstream and downstream reservoir volumes (V_1 and V_2, respectively) that are much larger than the interstitial rod volume V_r (i.e., $V_1 \gg V_r$ and $V_2 \gg V_r$). The assumption that $V_1 \gg V_r$ and $V_2 \gg V_r$ allows a "pseudo-steady-state" approximately of the gas flow dynamics in the SNF and avoids the need to consider pressure and flow transients in both the rod and upstream/downstream pressure reservoirs.

Thus, with the conceptual model provided by Coulson and Richardson (1997), the single-channel hydrodynamic flow approximation for complex media, and the pseudo-steady-state approximation for gas flow with dynamic pressure conditions at the rod boundaries, it is possible to extend isothermal steady-state gas analysis to the dynamic conditions encountered in the gas communication testing apparatus described in Section 2.1. In the next section, these concepts will be combined with material/energy balances for the upstream and downstream reservoirs to provide a general set of expressions by which the time-scale and equivalent hydrodynamic diameter associated with gas release from SNF can be assessed.

2.2.2 PNNL Gas Communication Model

To develop a gas communication test specific model, the following enabling assumptions are made with respect to both the test system and underlying gas transport physics:

- The gas communication system consists of three gas-filled volumes that comprise the upstream reservoir, rod interstitial volume, and downstream reservoir. Pressure disequilibrium between the upstream (high) and downstream (low) pressure reservoir effects gas transmission through the rod until pressure equilibrium is established.
- All resistance to flow can be attributed to the SNF rod.
- The gas contained within the system is ideal and uniform in composition.
- Gas transmission through the rod is isothermal (at temperature T_o) and "pseudo-steady" such that $G = G(P_1, P_2, T_o)$ and both upstream and downstream chamber volumes, V_1 and V_2, respectively, are much larger than the rod interstitial volume V_r.
- Gas flow through the SNF microstructure may be approximated using a single microchannel approximation characterized by the rod length L and equivalent hydrodynamic diameter D.
- The upstream and downstream reservoirs have fixed temperature T_o.

---

[f] For a more complete review of equations for treating flow in porous media and capillaries (and their short-comings), the reader is referred to Chapters 13 and 15 in Dallavalle (1948).

- The upstream and downstream reservoirs are characterized by time-dependent pressures $P_1(t)$ and $P_2(t)$, respectively, and static volumes V_1 and V_2.[g] From these values, other reservoir-specific properties such as specific volume v or density ρ may be derived using the ideal gas relationship.
- No transfer outside the upstream, rod, or downstream volumes is allowed. Note: The case of discharge to atmosphere will be realized with $V_2 \rightarrow \infty$.

Using these assumptions, expressions for pressure reservoir dynamics and gas flow dynamics will be established in the subsections that follow.

2.2.2.1 Pressure Reservoir Dynamics

The total mass m of gas contained within the test system can be expressed as the sum of gas masses contained within the individual volumes such that:

$$m = m_1 + m_2 + m_r \qquad \text{Eq. (2.8)}$$

where m_1, m_2, and m_r are the mass of gas within the upstream, downstream, and rod volumes, respectively. From the ideal gas law:

$$m = \frac{1}{R_m T_o}(P_1 V_1 + P_2 V_2 + \overline{P}_r V_r) \qquad \text{Eq. (2.9)}$$

where $\overline{P}_r$ is the average pressure within the rod and falls between the upstream and downstream pressures (i.e., $P_2 \leq \overline{P}_r \leq P_1$). The rod volume negligible (i.e., $V_1 \gg V_r$ and $V_2 \gg V_r$) such that:

$$m \cong \frac{1}{R_m T_o}(P_1 V_1 + P_2 V_2) = m_1 + m_2 \qquad \text{Eq. (2.10)}$$

In closed configurations (where there is no mass transfer outside the test system), m is constant. As a result, Eq. (2.10) can be used to relate system end points (i.e., initial and equilibrium pressure condition):

$$P_1 V_1 + P_2 V_2 = P_1^o V_1 + P_2^o V_2 = P_e(V_1 + V_2) \qquad \text{Eq. (2.11)}$$

where the "o" superscript refers to the initial and final values of time dependent properties and P_e is the equilibrium pressure. The equilibrium pressure reached by the system is then:

$$P_e = y_1 P_1 + y_2 P_2 \qquad \text{Eq. (2.12)}$$

where y_1 and y_2 are the upstream and downstream volume fractions (with $y_1 + y_2 \cong 1$). Eq. (2.12) holds for any time in the pressure evolution process.

As defined previously, gas is transmitted from the upstream to downstream reservoir with a mass flow rate G, which is uniform across the rod under the assumed pseudo-steady flow conditions. This means that:

$$G = -\frac{\mathrm{d}m_1}{\mathrm{d}t} \qquad \text{Eq. (2.13)}$$

For a closed system with constant total mass m, Eq. (2.10) allows us to relate changes upstream and downstream conditions through:

$$\frac{\mathrm{d}m_1}{\mathrm{d}t} = -\frac{\mathrm{d}m_2}{\mathrm{d}t} \qquad \text{Eq (2.14)}$$

This, combined with the ideal gas law, yields the following expressions for upstream and downstream chamber dynamics:

---

[g] ORNL gas communication testing use a variable upstream volume to maintain constant pressure P_1 (Montgomery and Morris 2019). For brevity, the derivations in this section will not explicitly consider dynamics with variable volume V_1 and V_2.

$$V_1 \frac{\mathrm{d}P_1}{\mathrm{d}t} = -GR_mT_o \qquad \text{and} \qquad V_2 \frac{\mathrm{d}P_2}{\mathrm{d}t} = GR_mT_o \qquad \text{Eq. (2.15)}$$

2.2.2.2 Gas Flow Dynamics

In the current section, gas flow dynamics within the SNF rod are considered in terms of generalized gas flow equations for isothermal systems to provide an explicit expression of the form $G = G(P_1, P_2, T_o)$ to couple with Eq. (2.15). Substitution of expressions for G into Eq. (2.15) yields one or two ordinary differential equations (ODEs) that must be integrated to develop a description for how pressure (upstream/downstream) evolve with time. The ideal result from integration is an analytical expression, as it avoids the added complexity of both numerically integrating the combined expression and applying numerical minimization routines to determine best fit hydrodynamic parameters (like hydraulic diameter). For this reason, significant effort is made in the current section to identify the region in which SNF rod gas transmission flow is laminar, as this region yields a closed-form analytical solution of Eq. (2.15). Turbulent gas flow is avoided as it generally requires numerical solution of Eq. (2.15), and more importantly, depends strongly on the roughness of the microchannel.[h] It is not necessary to avoid choked flow; however, choked and unchoked flow regions must be treated using separate dynamics in laminar flow. As shown below, it is not necessary to distinguish choked and non-choked flow, as the conditions required to assure laminar flow generally exclude choked flow.

To simplify analysis of mass flows, a dimensional recast of Eq. (2.2) is used by defining the following scaling coefficients:

$$\Gamma = \frac{P_1^2}{R_mT_og^2} \qquad \zeta = \left(\frac{P_2}{P_1}\right)^2 \qquad \Lambda = \frac{4f_fL}{D} \qquad \text{Eq. (2.16)}$$

with $g = G/A$ being the mass flux. This yields a scaled gas flow equation of the form:

$$\Gamma = \frac{\Lambda - \hat{\alpha}\ln\zeta}{1-\zeta} \qquad \text{Eq (2.17)}$$

Eq. (2.17) is general in that it spans both turbulent and laminar flow regimes and can be used to assess the critical pressure ratio ζ_c at which flow becomes choked. Turbulent flow onset can be handled implicitly through generalized Fanning friction factors, such as the Churchill (1977) expression. Choked flow occurs when $\zeta \leq \zeta_c$ with ζ_c defined by the implicit relationship:

$$\frac{1}{\zeta_c} = \frac{\Lambda_c - \hat{\alpha}\ln\zeta_c}{1-\zeta_c} \qquad \text{Eq (2.18)}$$

Determination of the critical pressure ratio facilitates calculation of Γ and mass flow rate G:

$$\Gamma = \begin{cases} \frac{\Lambda - \hat{\alpha}\ln\zeta}{1-\zeta} & \text{when} \quad \zeta_c < \zeta \leq 1 \\ \frac{1}{\zeta_c} & \text{when} \quad \zeta \leq \zeta_c \end{cases} \qquad \text{Eq. (2.19)}$$

$$G = \frac{P_1A}{\sqrt{\Gamma\, R_mT_o}} \qquad \text{Eq. (2.20)}$$

While the functional form of Eq. (2.20) looks straightforward, the dependence on Γ on the pressure ratio ζ is non-linear (due to the natural logarithm term) and the scaled friction factor Λ depends implicitly on the mass flow rate. Some simplification can be achieved by considering the relative magnitude of terms for microchannel flow. Typical SNF microchannel hydrodynamic diameters are on the order of 100 μm or

---

[h] In general, analysis of turbulent and secondary flows is avoided when quantifying underlying flow properties such as viscosity or hydraulic diameter. Indeed, a prime example is fluid rheometry/viscometer, which restricts itself to laminar flow configuration when assess fluid flow properties such as viscosity (see Steffe 1996). For the current application, restricting analysis to laminar flow has the added benefit that microchannel roughness need not be considered or estimated to enable analysis of hydraulic diameter [assuming that sufficient data fall within the laminar region allow said analysis].

less. Furthermore, while SNF rod lengths are typically on the order of 12 ft (3.6 m), current test lengths are on the order of 36 to 42 in. (0.9 to 1.1 m). Assessment of a typical fanning friction factor is difficult, but they generally are on the order of 0.01 or larger for current tests. From these estimates, a typical value for scaled friction can be derived:

$$\Lambda = \frac{4\,(10^{-2})\,(1\text{ m})}{10^{-4}\text{ m}} = 400$$

The pressure differences driving flows are largest at the start of the gas communication experiments. Different pressures evaluated in the current test program are bounded by upstream pressures of 750 psia (5.2 MPa) discharging to atmosphere 14.7 psi (0.1 MPa). This bounds the smallest ζ evaluated herein at:

$$\zeta = \left(\frac{0.1}{5.1}\right)^2 \sim 0.0004$$

thus, the term $-\ln\zeta \sim 8$ such that $\Lambda \gg -ln\zeta$. In practical terms, this means that microchannel flow is dominated by frictional losses (as one might expect given the ratio of crack diameter to rod length). From a phenomenological perspective, this reduces Eqs. (2.18) and (2.19) to:

$$\zeta_c = \frac{1}{1+\Lambda_c} \sim \frac{1}{\Lambda_c} \qquad \text{Eq (2.21)}$$

$$\Gamma = \begin{cases} \frac{\Lambda}{1-\zeta} & \text{when} \quad \zeta_c < \zeta \le 1 \\ \Lambda_c & \text{when} \quad \zeta \le \zeta_c \end{cases} \qquad \text{Eq. (2.22)}$$

From Eq. (2.21), one can estimate a typical pressure ratio for choked flow in friction-dominated SNF microchannel flows. Assuming a similar critical scaled friction factor of $\Lambda_c \sim 400$ as estimated under typical flow conditions, onset of choked flow occurs at a critical pressure ratio of:

$$\zeta_c = \left(\frac{1}{400}\right) \sim 0.0025$$

As estimates of the initial pressure ratio place $\zeta \sim 0.004$, it is unclear (given the potential for variation in the assumed parameters) if the initial mass flows are choked or not. However, based on the estimates above, it should be expected that a significant portion of the pressure rise or decay events will occur outside of choked flow.

The final complicating factor relates to the flow regime: The friction factor shows substantially different dependence on mass flow (as captured through the Reynold’s number). For laminar flows, the friction factor is:

$$f_f = \frac{16}{\text{Re}} \qquad \text{Eq. (2.23)}$$

For turbulent flows, the friction factor can be approximated as:

$$f_f = \frac{0.079}{\text{Re}^{0.25}} \qquad \text{Eq. (2.24)}$$

And for both Eqs. (2.23) and (2.24):

$$\text{Re} = \frac{gd}{\mu} \qquad \text{Eq. (2.25)}$$

As Reynolds number and turbulence are maximized when flow is maximized, flow will be most turbulent at the start of pressure equilibration. Taking the maximum, choked flow conditions as $\Gamma_c = \Lambda_c$, and assuming $T_o = 25$ °C (298.15 K), $R_m = 208$ J kg^{-1}K^{-1} (for argon), and $\mu = 24.2 \times 10^{-6}$ Pa s (for argon at T_o), then:

$$g = \frac{(5.1 \times 10^{6}\ \mathrm{Pa\ s})}{\sqrt{(400)\ (208\ \mathrm{J\ kg^{-1}K^{-1}})(298.15\ \mathrm{K})}} = 1024\ \mathrm{kg\ m^{-2}\ s^{-1}}$$

$$\mathrm{Re} = \frac{(1000\ \mathrm{kg\ m^{-2}\ s^{-1}})\ (1 \times 10^{-4}\ \mathrm{m})}{(24.2 \times 10^{-6}\ \mathrm{Pa\ s})} = 4132$$

The latter suggests that initial gas communication flows will be turbulent and that turbulence can persist through the gas communication process. Taking other parameters as fixed, laminar conditions should be achieved when the upstream pressure P_1 falls to half of its initial value (~2.5 MPa). This means that laminar flow will generally be available during typically observed gas communication test conditions here (where pressure is monitored from the start of the test until establishment of steady pressure conditions measurable within the accuracy of the pressure gage).

Given the estimates for choked and turbulent flow regimes made above and in the preceding pages, laminar unchoked flow dynamics can be expected to occur over a significant portion of the gas communication test. However, given the proximity of the initial test conditions to the cut-offs for both turbulent and choked flow regions, the gas communication data will need to be explicitly assessed to avoid inclusion of choked/turbulent data. For unchoked laminar flow, Eq. (2.22) reduces to:

$$G = \frac{\pi D^4}{256 \mu R_m T_o} \left(\frac{P_1^2 - P_2^2}{L} \right) \qquad \text{Eq. (2.26)}$$

Here, the flow area A is taken to be $A = \pi D^2/4$. Eq. (2.26) is a variant of Poiseuille's Law for compressible fluids [see Muskat (1934); Wutz et al. (1997)].[i] Eq. (2.26) can be used in conjunction with Eq. (2.15) and corresponding initial conditions for upstream and downstream pressure to solve for exact expressions of system pressure as functions of time. These expressions, and their scaling, are discussed in the subsection that follows. These expressions can be used in conjunction with experimental test data to derive metrics for SNF gas transmission, including transmission time-scales and equivalent hydrodynamic diameters. Substitution of Eq. (2.26) into Eq. (2.15) yields a set of first order differential equations for P_1 and P_2:

$$V_1 \frac{\mathrm{d}P_1}{\mathrm{d}t} = -\frac{\pi D^4}{256 \mu L} \left(P_1^2 - P_2^2 \right) \quad \text{and} \quad V_2 \frac{\mathrm{d}P_2}{\mathrm{d}t} = \frac{\pi D^4}{256 \mu L} \left(P_1^2 - P_2^2 \right) \qquad \text{Eq. (2.27)}$$

2.2.2.3 Gas Communication Pressure Dynamics

The approach taken to solve one or both of the equations depends on the type of test being evaluated. PNNL gas communication testing looked at two different types of tests:

1. **Balance testing** – The system is initially vented to atmosphere. Then, the upstream pressure reservoir is isolated and pressurized to an initial pressure of ~740 psia (5.1 MPa). Next, the rod and downstream volume are isolated from the atmosphere. Finally, the valve isolating the upstream volume from the rod and downstream reservoir is opened and the upstream and downstream volumes allowed to come to pressure equilibrium. The rate at which pressure equilibrates is governed by gas transmission through the SNF rod (and is what we seek to characterize). To facilitate characterization, the pressure evolution of both upstream and downstream volumes is monitored throughout the last step to provide experimental data to which the current modeling efforts can be applied.
2. **Decay testing** – Immediately following the balance test above, the valve isolating the downstream reservoir from the atmosphere is opened, effecting rapid depressurization of the

---

[i] Wutz et al. (1997) provides the exact isothermal expression used here. The expression developed by Muscat (1937) represents a generalize case of Eq. (2.26) for both isothermal and non-isothermal flow.

downstream reservoir to atmospheric pressure. Gas transmission through the SNF rod greatly limits the rate of upstream reservoir depressurization and can be characterized by monitoring the rate at which the upstream pressure “decays” to atmospheric pressure. Measurement of the upstream pressure as a function of time during pressure decay provides experimental data by which the gas transmission metrics (decay time-scale and hydrodynamic diameter) can be assessed using the models presented herein.

As a means to determine if the PNNL test data on a ¼-length rod using a different experimental setup is comparable to a full-length rod following a different methodology, the current report also seeks to evaluate ORNL data (Montgomery and Morris 2019) for comparison. The specific ORNL data evaluated herein involves pressurizing a downstream volume (initially at atmospheric pressure) from an upstream pressure reservoir held at constant pressure throughout the pressure equilibration process. The following paragraphs discuss, in brief, the approaches used to solve Eq. (2.27) for each of the three experimental scenarios, namely the PNNL balance and decay gas transmission and ORNL pressurization gas communication, and final analytical equations results from solution.

For PNNL balance testing, upstream and downstream pressure both vary during pressure evolution. As P_1 and P_2 variation is related by Eq. (2.12), only one ordinary differential equation from Eq. (2.27) needs to be solved. Furthermore, application of select pressure and time scaling factors reduces both coupled ODEs for P_1 and P_2 to a single ODE. The appropriate scaling factors for pressure balance testing are:

$$\phi_1 = \frac{y_1}{y_2} + \left(1 - \frac{y_1}{y_2}\right)\left(\frac{P_1}{P_\mathrm{e}}\right) \qquad \text{and} \qquad \phi_2 = \frac{y_2}{y_1} + \left(1 - \frac{y_2}{y_1}\right)\left(\frac{P_2}{P_e}\right) \qquad \text{Eq. (2.28)}$$

$$\tau = t/t_o \qquad \text{with} \qquad t_o = \left[\frac{128 y_1 y_2 \mu (V_1 + V_2) L}{\pi D^4}\right]\frac{1}{P_e} \qquad \text{Eq. (2.29)}$$

This renders $\phi_1 = \phi_2 = \phi$ and yields a scaled ODE of the form:

$$\frac{\mathrm{d}\phi}{\mathrm{d}\tau} = \frac{1}{2}(1 - \phi^2) \qquad \text{Eq. (2.30)}$$

Given initial pressure P_1^o and P_2^o (or ϕ^o in scaled form), the solution to Eq. (2.30) is:

$$\phi = \frac{1 - \theta e^{-\tau}}{1 + \theta e^{-\tau}} \qquad \text{with} \qquad \theta = \frac{1 - \phi^o}{1 + \phi^o} \qquad \text{Eq. (2.31)}$$

While the benefits of the scaled problem may not be immediately obvious, their utility will become apparent in treating the remaining test configurations.

PNNL decay testing involves opening the downstream reservoir to the atmosphere. In modeling terms, this can be approximated by letting $V_2 \rightarrow \infty$ such that the time rate change in P_2 becomes zero (i.e., $P_2 = P_2^o = \text{const}$). Treatment of Eq. (2.27) need only consider P_1 dynamics. Application of the following PNNL decay pressure and time scaling factors, namely,

$$\phi = \frac{P_1}{P_2^o} \qquad \text{and} \qquad t_o = \left(\frac{128 \mu V_1 L}{\pi D^4}\right)\frac{1}{P_2^o} \qquad \text{Eq. (2.32)}$$

yields an ODE of the form given by Eq. (2.30). As is expected, solution of this ODE produces the same analytical expression Eq. (2.31).

Finally, in the ORNL pressurization testing, the upstream pressure is fixed such that $P_1 = P_1^o$. Then, the downstream pressure increases until equilibrium is established. Similar to the approach for PNNL balance and decay, application of the following ORNL pressurization specific pressure and time scaling factors, namely,

$$\phi = \frac{P_2}{P_1^o} \qquad \text{and} \qquad t_o = \left(\frac{128 \mu V_2 L}{\pi D^4}\right)\frac{1}{P_1^o} \qquad \text{Eq. (2.33)}$$

yields an ODE of the form given by Eq. (2.30) whose solution produces the same analytical expression as Eq. (2.31). Thus, the scaled dynamics for all gas communication tests considered herein can be treated using a single analytical expression, Eq. (2.31), so long as analysis is constrained to laminar, unchoked flow regions.

The analysis methodology is relatively straightforward. Gas communication test data collected before, during, and after gas transmission can be used to assess relevant values for P_1^o, P_2^o, and P_e (along with y_1 and y_2 if needed). Next, measured pressure data are scaled to provide ϕ as a function of unscaled time t [i.e., $\phi = \phi(t)$]. Finally, non-linear regression can be used to assess the value of t_o that best scales $\phi = \phi(t)$ in accordance with Eq. (2.31). In cases where access to measured gas communication electronic data is not available, the time constant is assessed by finding the mid-point of the pressure evolution ϕ_m as determined by rescaling:

$$\phi_m = \frac{1+\phi^o}{2} \qquad \text{Eq. (2.34)}$$

into absolute pressure and finding the mid-point time t_m at which this pressure falls. Then:

$$t_o = t_m \left[\ln\left(\frac{3+\phi_o}{1+\phi_o}\right)\right]^{-1} \qquad \text{Eq. (2.35)}$$

The measured time scaling constant provides a link between the experimental conditions (pressure and volumes) to the hydrodynamic diameter and permeability. Individual estimates of t_o must be interpreted per its base scaling equation, namely Eqs. (2.29), (2.32), and (2.33), for PNNL balance, PNNL decay, and ORNL pressurization tests, respectively. These equations may be solved for hydrodynamic diameter D. For example, the hydrodynamic diameter estimated from time-constants for PNNL decay testing is:

$$D = \left(\left(\frac{128\mu V_1 L}{\pi t_o}\right)\frac{1}{p_2^o}\right)^{1/4} \qquad \text{Eq. (2.36)}$$

As applied to SNF, Eq (2.36) expresses the resistance to flow through the tortuous flow channel formed by fuel cracks and inter-pellet spacing as a single representative diameter. The resistance to permeable media flow can similarly be expressed in terms of flow permeability K. For capillary flow, an expression relating permeability to hydraulic diameter can be readily derived from comparison of Poiseuille’s and Darcy’s law [see Eq. 13-13 in Dallavalle (1948)]. This expression is:

$$K = \frac{D^2}{32} \qquad \text{Eq. (2.37a)}$$

It should be noted that Eq. (2.37a) represents an unnormalized form of the permeability based on the true capillary area (rather than the cross-section area of the porous flow medium). A “normalized” permeability K_n can be defined that considers the total cross-sectional area of medium. It is given by:

$$K_n = \epsilon K \qquad \text{Eq. (2.37b)}$$

where ϵ is the void fraction of the fuel. Equations (2.28) through (2.37) provide a complete set of equations by which SNF gas transmission and gas transmission metrics may be assessed. In the section that follows, PNNL and ORNL gas transmission data for SNF rods are evaluated using these equations. For the current report, only hydraulic diameter D and unnormalized permeability K will be evaluated.

2.3 Results

This section describes the results of PNNL and ORNL gas communication testing from rod/rod segments described in Table 2-1. In particular, analysis of balance and decay testing for PNNL rod segment UL-4 from rod 6U3L08 is provided; analysis of selection ORNL pressurization testing from rod 30AK09 is also included.

Table 2-1. Description Gas Communication Rod Samples Analyzed

Test Location	Assembly/Rod Identification	Clad Type	~ Rod-Average Burnup (GWd/MTU)	Sample Subset	Location from Bottom of Rod
ORNL	30AK09	M5®	53	Entire Rod	NA
PNNL	6U3L08	ZIRLO®	55	UL-4	21 – 926 mm

2.3.1 Analysis of ORNL Data for Rod 30AK09

ORNL gas communication testing of rod 30AK09 has been reported in Montgomery and Morris 2019. The current analysis of limited SNF rod pressurization data from Montgomery and Morris 2019 serves a dual purpose: 1) to validate the ability of the analysis proposed in Section 2.2 to determine physically reasonable hydraulic diameters[j] and 2) to provide a means of validating current test and test analysis protocols for PNNL sibling pins against publicly-available, peer-reviewed gas communication data for nominally equivalent SNF rods. Montgomery and Morris 2019 report gas communication in terms of normalized permeability. Equation (2.37) could be used to develop estimates for hydraulic diameter from permeability measurements; however, the pressurization time constants t_o (as determined by pressure mid-points) are used instead to insure consistent use of representative gas temperatures and viscosities between the current calculations and PNNL analysis of Rod Segment UL-4 from the 6U3L08 rod.

Rod pressurization testing data are provided in Figure 8 of Montgomery and Morris 2019, which is reproduced below in Figure 2-3 along with additional analysis by PNNL; this figure shows the evolution of the rod downstream pressure as a function of time after the upstream rod volume is pressurized to 1.41, 2.17, and 2.89 MPa, respectively. To analyze these data, the time to reach mid-point of the pressure evolution (i.e., t_m) is evaluated directly from Figure 2-3 and used to calculate the pressurization time constant t_o via Eq. (2.35). This analysis is shown in Figure 2-3 using solid red, blue, and green lines for P_1 of 2.89, 2.17, and 1.41 MPa, respectively. The results of this analysis are also tabulated in Table 2-2. For ORNL pressurization testing, the time constant t_o and initial upstream pressure P_1^o are related by Eq. (2.33). The hydraulic diameter D can be determined by:

$$D = \left(\left(\frac{128\mu V_2 L}{\pi t_o}\right)\frac{1}{P_1^o}\right)^{1/4} \qquad \text{Eq. (2.38)}$$

---

[j] Here, validation of the hydraulic diameter is effected by comparison of the model-estimates to visual estimates of crack dimensions in SNF rod cross-sectional images provided in Montgomery and Morris 2019.

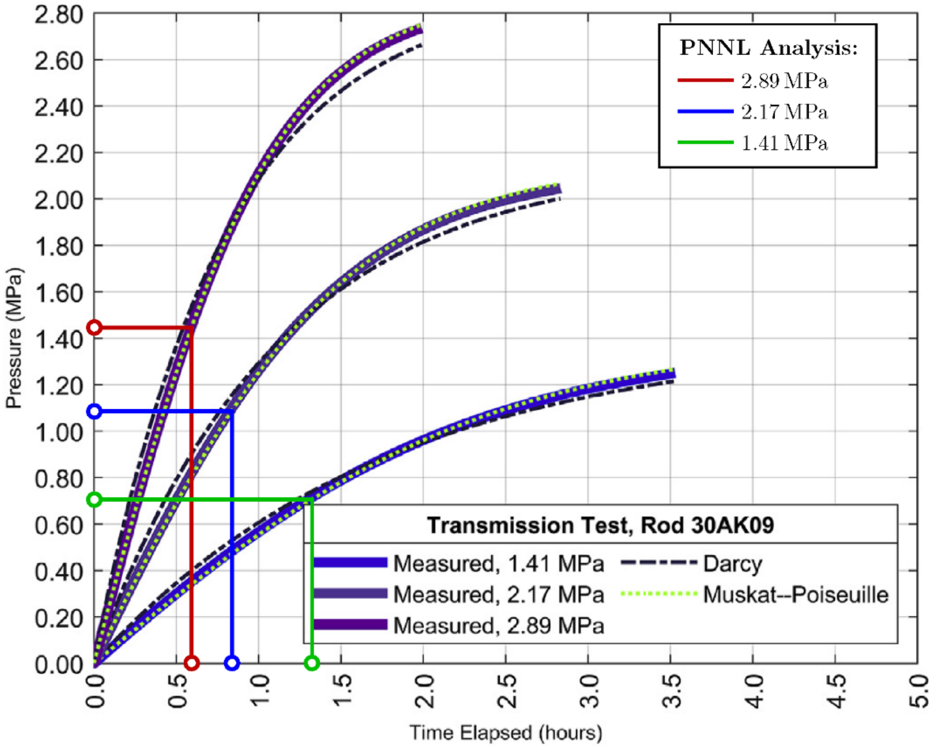

Figure 2-3. ORNL Pressurization Data for Rod 30AK09 Taken from Montgomery and Morris 2019, Figure 8.

Figure Note: For the current report, PNNL analyzes the pressurization time constant t_o *by determining the time* t_m *to reach the pressure mid-point* P_m*. The solid red, blue, and green lines trace the mid-point pressures to the mid-point times for upstream pressures of 2.89, 2.17, and 1.41 MPa, respectively. The data derived from this analysis are tabulated in Table 2-2.*

Table 2-2. Analysis of Time Constants Derived from Figure 2-3 Analysis from ORNL Rod 30AK09 Pressurizations Test Data Reported in Montgomery and Morris 2019.

P_1^o (MPa)	ϕ^o	t_m (hr)	t_o (hr)	D (µm)	K (m^2)
1.41	0	0.591	0.538	67.8	1.44×10^{-10}
2.17	0	0.835	0.760	68.3	1.46×10^{-10}
2.89	0	1.32	1.20	69.3	1.50×10^{-10}

Table Note: The mid-point times are read directly from Figure 2-3 and converted to representative time constants t_o *using Eq. (2.35).*

Finally, rod permeability K can be determined using Eq. (2.37). Estimates for rod 30AK09 hydraulic diameter D and permeability K are derived from Figure 2-3 time constants t_o using Eqs. (2.37) and (2.38) and are reported in Table 2-2. Conversion of t_o to D and K assumes argon as the communication gas, a rod downstream volume and length of 37.7 mL and 3.65 m, respectively (taken from Table 5 in

Montgomery and Morris 2019), an initial downstream pressure $P_2^o = 0$,[k] and a gas viscosity of 23.0 µPa s (predicted using the correlation of Lemmon and Jacobsen (2004) at an assumed gas temperature of 25°C[l]). The results suggest a relatively uniform hydraulic diameter of ~68 µm and permeability of ~1.45 × 10^{-10} m^2, irrespective of test pressure. While the results suggest that hydraulic diameter increases with test pressure, it is unclear if this relates to some defect in the analysis (or underlying assumptions), such as the inclusion of periods of choked flow in determining t_o, or if it relates to a physical process such as expansion of the fuel or cladding under increased internal pressure or erosion of the cracks by gas flow. It should be noted that the ~1-µm increase in hydraulic diameter observed in Table 2-2 as test pressure increases from 1.41 to 2.89 MPa is similar in magnitude to increases in SNF rod diameter observed in PNNL pressure and optical micrometer testing. In particular, PNNL has pressurized rod segment UL-4 to ~5 MPa (725 psi); the increase in UL-4 rod diameter as a result of pressurization (as measured by optical laser micrometry) was ~2.5 µm. As such, it is plausible that the ~1-µm increase in hydraulic diameter observed here is associated with expansion of the hydraulic path under increased pressure and not simply an artifact of measurement uncertainty or underlying violation of model assumptions during testing.

In more general terms, the hydraulic diameter estimated for rod 30AK09 from the methods outlined above seems reasonable. Estimates of crack diameter made by direct visual examination (cf. Fig 1c in Montgomery and Morris 2019) suggest crack widths in the range of 100 to 200 µm, which would lead to hydraulic flow diameters ranging from 200 to 400 µm (assuming parallel plate geometry). That the measured effective hydraulic diameter (~68 µm) is smaller is not surprising. As noted earlier, the enabling assumption of single-channel flow generally render estimates of effective flow diameter smaller than the dimensions observed through direct visual observation. Moreover, the effective hydraulic diameter estimated from the single-channel approach generally corresponds to the smallest, most restrictive internal diameters. As such, the current method appears to provide reasonable, order-of-magnitude estimates of internal hydraulic diameters for SNF.

2.3.2 Analysis of PNNL Data for Rod Segment UL-4

PNNL performed gas communication testing on rod segment UL-4 from rod 6U3L08. Two separate tests of the rod segment were conducted and comprised single pressure balance and decay tests. For balance testing, the upstream rod volume was pressurized to ~740 psia (5.1 MPa, which represents the upper range of room temperature end of life rod internal pressures for standard, modern 17×17 fuel rods) and allowed to fill the downstream rod volume (initially at atmospheric pressure). The results, including a fit of the data to Eq. (2.30) [with pressure scaling defined by Eqs. (2.28) and (2.29)], of this single balance test are presented in Figure 2-4. Following this test, the rod was vented (decay) to atmosphere. The results of the decay test, including a fit of the data to Eq. (2.30) as before but with pressure scaling defined by Eq. (2.32), are presented in Figure 2-5. In both cases, fits have been iterated to exclude regions of choked and turbulent flow. Iterative analysis finds all the roughly 600 seconds worth of balance data fall in the laminar, unchoked flow regime.[m] Evaluation of the decay testing finds that flow is laminar throughout

---

[k] ORNL testing initially applied vacuum to the downstream end of the rod, which is approximated as $P_2 = 0$ in the current analysis. It should be noted that application of vacuum to initialize the downstream conditions guarantees that the initial gas communication will be choked. While the current analysis only considers the mid-point of the pressure rise (which excludes the choked flow region), the initial choked dynamics will limit gas flow during the initial portion of depressurization, and thus delay achievement of the mid-point pressure and increase observed t_o. No attempt is made to quantify the impact choked flow has on interpretation of the ORNL results in the current report.

[l] The hot cell temperature was monitored throughout testing generally fell between 28-32°C. Use of a single representative error of 25°C leads to differences of <1% in reported permeabilities and hydraulic diameters and is not considered to be a significant source of result uncertainty.

[m] Fits of the decay data consider the initial condition to be the first observed condition where flow remains both unchoked and laminar. Under this approach, exclusion of choked/turbulent flow region data does not introduce error in the time constant t_o derived from non-linear regression.

the entire 20 hours of testing and choked during the first 7.5 minutes of testing. As such, the first 7.5 minutes of decay testing data were excluded from time constant analysis discussed below.

The time constants t_o associated with pressure balance and decay testing of rod segment UL-4 are determined by fitting the pressure evolutions in Figure 2-4 and Figure 2-5 using Eq. (2.30) and the appropriate pressure scaling. Interpretation of pressure balance tests requires evaluation of the equilibrium pressure P_e and relative upstream and downstream volume fractions y_1 and y_2 from test data using Eq. (2.12). In addition, test-specific parameters such as the upstream volume V_1 (assumed to be 200 mL for the current analysis based on system knowledge) and rod segment length (36 in. / 0.91 m). Analysis of PNNL test data for rod segment UL-4 assumes helium as the carrier gas [with viscosity determined by Flynn et al. (1963)] at a representative temperature of 25°C. Interpretation of decay testing requires only knowledge of the upstream volume, rod length, and atmospheric pressure. Finally, assessment of initial system pressures P_1^o and P_2^o depends on the range of data analyzed (i.e., the range in which pressures are both unchoked and laminar). The general approach to fitting data involves the following steps:

1. Data are selected based on the recorded timestamps associated with gas communication pressurization / depressurization.
2. The test data and test data end points are used to assess representative values for P_1^o, P_2^o, P_e, y_1, and y_2.
3. The pressure data are scaled using Eq. (2.28) for balance and Eq. (2.32) for decay and fit to Eq. (2.30) to determine the appropriate time constant t_o.
4. The time constant is used to assess hydraulic diameter D, which enables calculation of the Reynolds number for flow and the critical pressure ratio for choked flow.
5. Data are refined to remove any turbulent/choked flow data using the Reynolds number and choked flow analyses from the previous step.

Steps 2 through 5 are subsequently repeated until the hydraulic diameter converges to a single value. The tabular results of this analysis are presented in Table 2-3.

Table 2-3. Tabulated Results of Analysis of Balance and Decay Pressure Testing of PNNL Rod Segment UL-4.

Parameter	Balance Test Value	Decay Test Value
Upstream Volume Fraction y_1	0.994	NA
Downstream Volume Fraction y_2	0.006	NA
Initial Upstream Pressure P_1^o, psia	735(a)	585(b)
Initial Downstream Pressure P_2^o, psia	14.1	15.1
Equilibrium Pressure P_e, psia	732	15.1
Hydraulic Diameter D, μm	46.2	75.2
Permeability K, m^2	6.68×10^{-11}	1.77×10^{-10}
Normalized Permeability, K_n, m^2	3.54×10^{-15}	2.48×10^{-14}
Fit Coefficient of Determination R^2	0.9996	0.9921

(a) Corresponds to the start of the fit region for balance testing. Initial test pressure was 736 psia.

(b) Corresponds to the start of the fit region for decay testing. Initial test pressure was 730 psia.

Table Note: Balance results correspond to data developed from analysis of the pressure evolution shown in Figure 2-3. Decay results correspond to data developed from analysis of the pressure evolution shown in Figure 2-4.

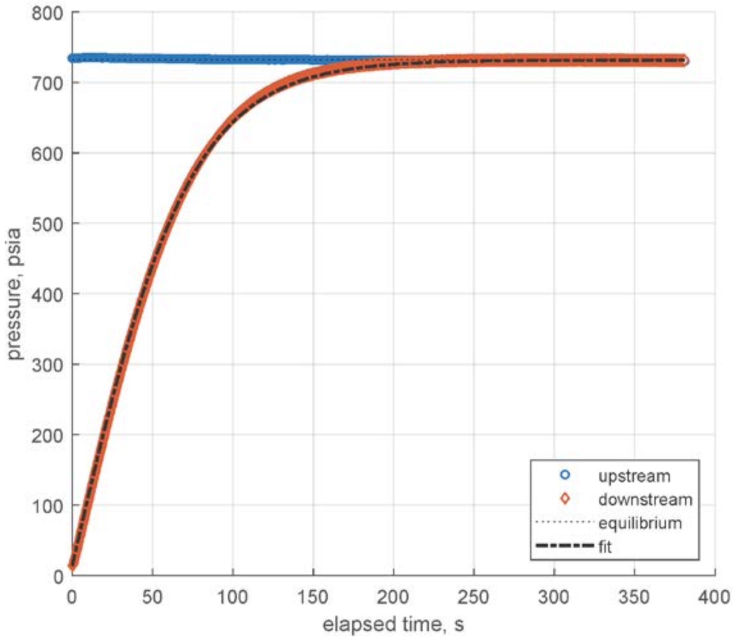

Figure 2-4. PNNL Pressure Balance Data for Rod Segment UL-4.

Figure Note: Graph shows both the evolution of upstream pressure P_1 *(blue circles) and downstream pressure* P_2 *(orange diameters). The downstream pressure is modeled using Eq. (2.30) with pressure scaled by Eq. (2.28) [dashed-dotted line]. The inferred equilibrium pressure is shown by the dotted line. Given that the upstream volume is substantially (by two orders of magnitude) larger than the downstream volume, the upstream pressure is nearly constant throughout pressure equilibration.*

Evaluation of the fits presented in Figure 2-4 and Figure 2-5 demonstrate that Eq. (2.30) coupled with the proper test pressure scaling and an appropriately selected time constant t_o provide an adequate fit of the pressure evolution data. In general, the balance test fit is better than that for the decay fit (with an R^2 value for each of 0.9996 and 0.9920, respectively). The poorer fit on the decay test manifests as a slower predicted decay than that experimentally observed. Possible causes for this discrepancy include potential leaks in the system, contraction of the system at reduced pressure, or measurement errors in pressures (which become more significant as the pressure differential approaches zero at long times); however, insufficient data exist to determine the exact cause in the current analysis.

Inspection of the tubular results derived from the pressure evolution data finds hydraulic diameters for the decay and balance testing of 46.2 and 75.2 µm, respectively. In terms of overall magnitude, these results are comparable to that determined from ORNL rod 30AK09 of 68 µm. Similarity in the PNNL/ORNL hydraulic diameters suggests that segmentation of the rod in the current testing did not grossly impact rod permeability; however, more conclusive statements on lab-to-lab test variability and test approach impacts on measured permeabilities will require a more complete set of rod permeability data from PNNL.

Direct comparison of UL-4 hydraulic diameters derived from PNNL balance and decay testing evidences a significant ~30-µm difference. An immediate cause for this large disparity is not clear. It is possible that application of pressure during the balance and leading up to the decay test expands the fuel (or increases the gap between the fuel and cladding), resulting in the higher decay diameter measured. Indeed, hydraulic diameter expansion was observed in the analysis of ORNL data discussed in the preceding section, where a pressure increase from 1.41 to 2.89 MPa saw a corresponding increase in hydraulic diameter from 67.8 to 69.3 µm. However, the ~1-µm increase observed in ORNL data is minor compared to the near ~30-µm increase (46.2 to 75.2 µm) observed in PNNL testing. Moreover, it does not seem possible to attribute the disparity in balance and decay test diameters to increased test pressure alone (ORNL testing reaches a 2.89-MPa maximum pressure, whereas PNNL reaches 5.1 MPa), as it is nearly an order of magnitude greater than the ~2.5-µm increase in the diameter of rod UL-4 characterized by optical micrometry at 5.0 MPa. While the latter observation rules out rod expansion, increases in the hydraulic diameter can still be attributable to changes in the internal structure of the fuel itself (e.g., shifting of the fuel or erosion of the hydraulic path). Likewise, defects in the test apparatus (such as slow leaks) could also contribute to the appearance of increased hydraulic diameter and permeability of the rod to gas flow. Of concern is the limited volume of the downstream reservoir in the balance test, which (as designed) including only the tubing volume, filter housing volume, and valve volume. Analysis of the balance equilibration dynamics using measured upstream and downstream pressures suggest a downstream volume of ~ 1 mL; best estimates of the internal fuel porosity place actual fuel void volume (i.e., the aggregate volume formed by the gaps between and cracks within the fuel pellets) on the order of 0.1 mL or less. As such, the assumption that $V_2 \gg V_r$ holds in balance testing (albeit to a much smaller extent than the ~200 mL upstream volume).

Given the arguments/discussion above, resolution of the exact cause for the observed hydraulic diameter from the current (single set of balance and decay test) data is not immediately possible. Additional testing is needed to assess if either the increase in hydraulic diameter is permanent (suggesting a real change in internal structure) or reproducible (which would help confirm or rule out defects in the test apparatus itself).

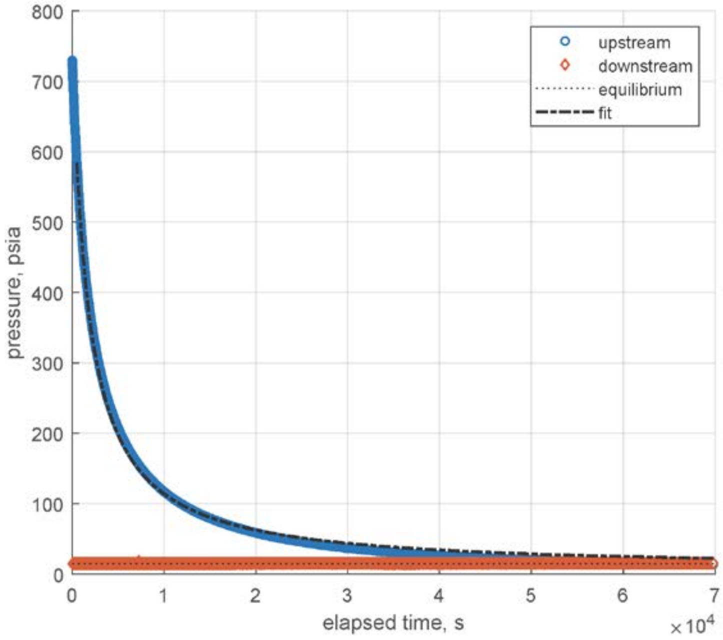

Figure 2-5. PNNL Pressure Decay Data for Rod Segment UL-4.

Figure Note: Graph shows both the evolution of upstream pressure P_1 *(blue circles) and downstream pressure* P_2 *(orange diameters). The upstream pressure is modeled using Eq. (2.30) with pressure scaled by Eq. (2.31) [dashed-dotted line]. The inferred equilibrium pressure is shown by the dotted line. The downstream volume is vented to atmosphere and is constant throughout upstream volume pressure decay. Note: The fit excludes the first 7.5 minutes of pressure decay as these data are assessed to correspond to choked/turbulent flow.*

2.4 Secondary Data

Gas communication testing is accompanied by secondary experiments used to quantify the degree of SNF rod diameter expansion during pressurization to ~5.0 MPa and the release of SNF from the rod to downstream components during depressurization. The latter is representative of fuel release from a gross breach (i.e., the fuel cross-section is exposed), although fuel transport may be constrained by downstream impinging surfaces. Both secondary tests are discussed in the sub-sections that follow.

2.4.1 Rod Diameter Measurements

Two high-speed optical micrometers (Keyence Model LS-9030, measurement range 0.08 to 30 mm, measurement accuracy ±2 µm, repeatability ±0.1 µm), installed at rod positions corresponding to 1/3 and 2/3 of the total rod length, were used to evaluate expansion of rod segment UL-4 during the gas communication pressurization (“balance”) testing. The rod diameter for Segment UL-4 was measured prior to pressurization, after equilibration at ~740 psia (5.1 MPa), and after depressurization. In addition, expansion measurements of empty fuel cladding (i.e., a “blank” rod) were also made to help isolate the effects of fuel/rod radiochemical history on the rod expansion. The blank rods were 17×17 assembly, non-irradiated, non-hydrided, as-manufactured cladding. Results of pressure expansion testing are provided in Table 2-4. The applied pressure of 5.1 MPa represents a 40% increase (seven standard deviations) over the EOL pressure of 3.6 ± 0.2 MPa (at 25°C) for rod UL inferred from gas puncture testing. In relative terms, the 5.1 MPa corresponds to a EOL storage temperature of approximately 145°C.

Table 2-4. Laser micrometer rod diameters measured for rod blanks and Rod Segment UL-4.

Rod	Pressure [MPa]	Initial Diameter [mm]	Pressurized Diameter [mm]	Final Diameter [mm]	Diameter Increase at Pressure [µm]	Depressurized Diameter Change [µm]
Rod Blank 1	5.0	9.5380	9.5407	-- --	2.7	-- --
Rod Blank 2	5.0	9.5356	9.5384	-- --	2.8	-- --
UL-4 Pos. 1	5.1	9.4168	9.4191	9.4170	2.3	0.2
UL-4 Pos. 2	5.1	9.4325	9.4352	9.4339	2.7	1.4

Table Note: Measurements were taken before pressurization (initial diameter), at pressure (pressurized diameter), and after depressurization (final) diameter. The increase in diameter at pressure and after depressurization are also reported.

The laser micrometer data indicate that rod pressurization to ~5 MPa increases the diameter by approximately 2.5 µm. The observed increase in rod diameter is the same for both the rod blank and Segment UL-4. Subsequent depressurization of the rod appears to reduce the diameter. Position 1 diameter measurements for UL-4 suggests a return to (more-or-less) the original rod diameter, whereas position 2 diameter measurements suggest a positive 1.4 µm variance following depressurization. The latter variance could suggest that pressurization yields a break in the fuel-clad bond. Moreover, such a permanent irreversible change in the internal structure of fuel is consistent with the observed increase in hydraulic diameter observed in gas communication testing. However, Table 2-4 observations are based on a single gas communication test, and as such, there is need to demonstrate the change is repeatable and not attributable to other test phenomenon (such as an axial shift in the fuel rod during pressurization such that the initial and final location of fuel being observed by the optical microscope are different) or measurement uncertainty to increase confidence in the assertion that pressurization does change the internal fuel structure.

2.4.2 Particle Release Measurements

Gas communication testing also took steps to evaluate and quantify particle release during rod depressurization (i.e., during gas communication decay testing). Methods for quantifying release involved installing a filter to collect solids entrained in the gas discharged from the SNF rod. Given the geometry of the grips used to hold the rod in place and the valves needed to isolate the rod from atmosphere, the filter could not be installed immediately at the grip discharge. The internal surfaces and impingement points that exists between the rod and the filter are expected to collect particulate released from the rod and prevent it from reaching the filter. To quantify the mass of fuel deposited prior to the filter, the downstream internal volume of the gas communication test system was first decoupled from the fuel rod and cleared by blowing air through the downstream volume.[n] Next, the internal surfaces were rinsed with a 6.75M nitric acid solution to dissolve any remaining fuel particles. Prior to UL-4 particle release testing, a high-pressure blowdown through a blank rod into a capture filter was conducted to provide a point-of-reference for UL-4 particle release testing (and to help isolate isotope contributions resulting from ambient hot-cell contamination). All tests employed a 47-mm-diameter, 0.1 μm PTFE filter manufactured by Advantec MFS, Inc.

The ^{134}Cs, ^{137}Cs, and ^{154}Eu activities in the UL-4 depressurization test filter, blowdown filter, and acid rinse solution was quantified by gamma energy analysis (GEA). As the acid rinse contained the majority of SNF release (see discussion in following paragraph), the ^{134}Cs, ^{137}Cs, and ^{154}Eu activities in the rinse were used to estimate the total fuel release using isotopic specific activity and estimated fuel isotopic contents. Table 2-5 provides a summary of the filter and rinse solution activities as measured by GEA. Activities for four gas commination “elements” are provided in Table 2-5:

- The pre-test blank tube blowdown – as discussed in the preceding paragraph, a blank tube was inserted into the gas communication system. A high-pressure blowdown through the system was collected on a filter to quantify isotopes resulting from ambient contamination.
- The UL-4 test filter activity – here the activity resulting from particles released from rod UL-4 and collected on the downstream filter is presented.
- The UL-4 post-test blowdown – as noted above, immediately following gas communication testing of UL-4 but before acid washing of system internals, a blank rod was inserted into the system with a clean filter. A high-pressure blowdown of the system was effected to assess the mobility of release fuel that had adhered to the system internals.
- The UL-4 test internal volume activity – represents the activity of particulate collected by acidic washing the system internals after depressurization of UL-4 and post-test blow down.

It should be noted that approximately 1/5th of the total rinse solution used to wash the volume leading to the filter was counted; as such, the UL-4 test internal volume activity (i.e., the right most column in Table 2-5) derived from GEA counting of the rinse solution has been increased by a factor of 5 to account for this fact. Other activities reported represent whole filter counting and do not need to be corrected.

Table 2-5. GEA Counting Results for Fuel Release during Depressurization of Rod Segment UL-4.

Isotope	Pre-Test Blank Tube Blowdown Activity [Bq]	UL-4 Test Filter Activity [Bq]	UL-4 Post-Test Blowdown Activity [Bq]	UL-4 Test Internal Volume Activity [Bq]
Co-60	0.0286	-- --	0.0983	20.3
Cs-134	-- --	3.50	-- --	14,050
Cs-137	-- --	65.8	0.235	330,500
Eu-154	-- --	0.176	-- --	835
Am-241	-- --	0.136	0.0983	690

---

[n] A new filter was installed to evaluate the fraction of particles derived from this step.

Table Notes: Counting results are shown for the downstream UL-4 depressurization capture filter, blow down filter, and internal volume holdup (determined by nitric acid rinse). For reference, the activity of a blank tube blowdown test is also included (a test which replicates UL-4 testing with an empty tube).

As shown by the Table 2-5 results, particulate capture on the internal volume leading up the filter appears to be approximately 10,000 larger than that which makes it to the filter. Moreover, analysis of the blowdown filter installed to collect particle release by air clearing after the fuel was decoupled (and before acid rinsing) evidences little if any particulate release. This suggests that the fuel particles that deposit immediately downstream of the rod are not easily mobilized. It should be noted that the total internal distance separating the end of the rod from the filter is estimated to be ~10 inches. A scaled drawing of the system volume downstream of the rod is given in Figure 2-6.

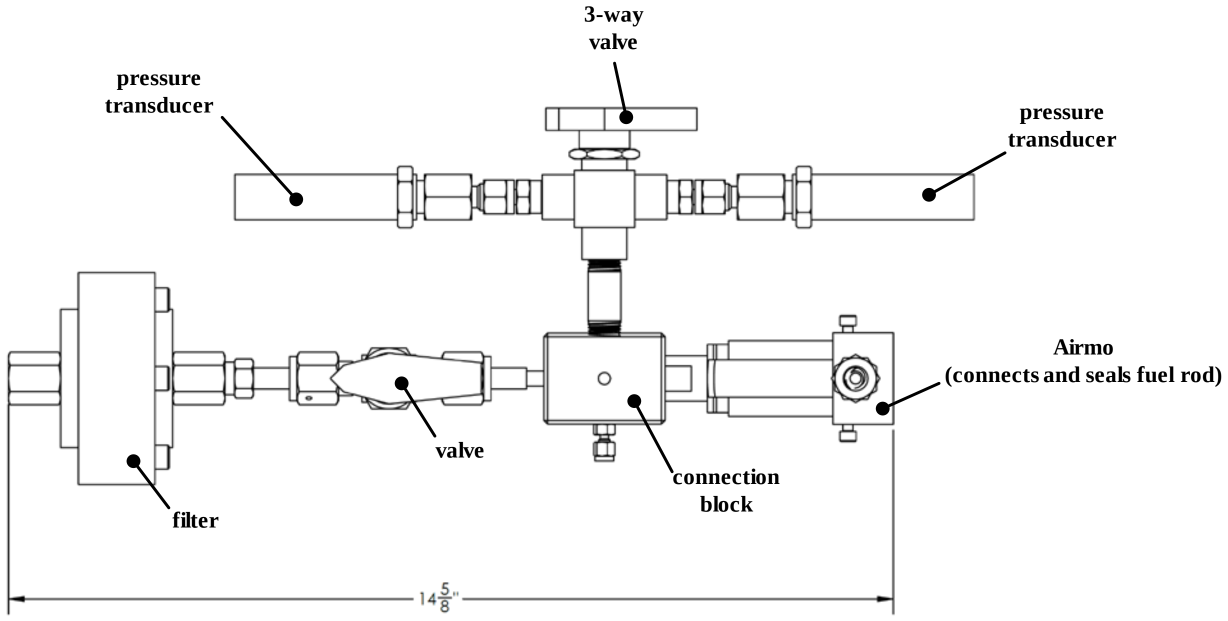

Figure 2-6. To-scale Drawing of the Volume Downstream of the Rod.

Figure Note: The fuel rod connects at the Airmo®.

As the internal volume appears to collect most of the particulate release, estimates of total release for rod segment UL-4 are based entirely on the internal volume activity. Estimates of total release based on ^{134}Cs, ^{137}Cs, and ^{154}Eu activities in this sample yield total aerosol fractional release in the range of 10^{-8} to 10^{-7} kg fuel release per kg fuel in rod. In comparison, Hanson et al. (2008) observed fractional releases ranging from 10^{-7} to 10^{-5} for HBU SNF. As such, the fraction released in the current testing seem in line with previous measurements of fuel release. It should be noted that the release observed in the current experiment is slow. The upstream volume stores approximately 200 mL of gas at 750 psia; given the small hydraulic diameter (79.5 um), release to atmospheric is slow and was monitored for 20 hours following testing (see Figure 2-5). During release, the maximum mass flow rate estimated to have occur was 1.0×10^{-6} kg s^{-1} and corresponded to the initial release under choked flow conditions.

As this was the first release test at high pressure, it was unclear how the fuel would distribute downstream of the rod. It was hoped the fuel would primarily collect on the filter, allowing for post-test quantification of released fuel particle size by direct imaging of particles collected on the filter. As demonstrated in Table 2-4, most particles do not collect on the filter. Given the disparity in activity between the system internal volume (where the particles do collect) and filter observed, it is unclear if any particulate that could be imaged on the filter would be representative of those that "plate out" upstream of the filter. Of course, acid dissolution of the internal volume destroys the particulates, rendering it impossible to determine the size of any particles plated out in Segment UL-4 testing. Modifications to the test system have been undertaken to enable collection of particulates immediately downstream of the rod so that future gas communication tests can be used to assess the size of released fuel.

2.5 Summary

The current section evaluated gas communication dynamics through two SNF rods. A gas communication test apparatus for characterizing gas communication dynamics was developed and is described herein. Next, a technical approach for interpreting pressure dynamics measured during gas communication testing was developed with the goal of characterizing the time scale for gas transmission and internal rod flow characteristics, namely hydraulic diameter and permeability. PNNL then used the gas communication model to evaluate flow characteristics associated with recent gas transmission data for rod 30AK09 collected by ORNL (Montgomery and Morris 2019) and gas transmission data for rod segment UL-4 tested using the gas communication system described herein. Analysis of the results finds that the models, when coupled with an appropriate selected time constant, provide a reasonable description of the pressure evolution dynamics. Further evaluation of the best-fit time constants finds effective hydraulic diameters for gas transmission on the order of 46.2 to 75.2 μm. The inferred gas flow diameters are consistent (on an order of magnitude basis) with SNF crack dimensions determined by visual inspection of SNF rod segment ends (presented in Montgomery and Morris 2019). The current gas communication results also evidence an increase in hydraulic diameter with increasing pressure in both PNNL and ORNL tests that could suggest SNF expansion or increased fuel/cladding debonding under increasing pressure.

The increase observed in analysis of ORNL data is consistent with increases in rod diameter determined by PNNL through direct optical laser micrometry. In contrast, the increase in hydraulic diameter observed in PNNL testing of rod UL-4 is an order of magnitude larger than expected from rod expansion under pressure alone. As the gas communication testing data are limited to a single set of balance and decay tests for rod UL-4, it is not possible to isolate a root cause for the large increase in hydraulic between the two UL-4 gas communication tests. Regardless, the results of the current study provide descriptors of the internal flow structure that should allow estimation of time-scales for SNF depressurization under prototypic conditions. As the current study uses upstream volumes on the order of 200 mL, the time constants associated with pressure decay are typically much longer than would be observed in real systems (where the volume can be on the order of 1 to 20 mL depending on the point of breach and the path the gas in the plenum has to take to reach the breach). While the current analysis does not attempt to calculate the time-scales associated with breaches with representative rod volumes, the methods provided herein are sufficiently general to enable such calculations given the hydraulic diameters measured herein. Follow-on work will employ these methods to estimate the rate of pressure decay and gas release from SNF breaches with representative gas inventories.

This page is intentionally left blank.

3. FUEL DISSOLUTION

As outlined in Saltzstein et al. 2018, PNNL is to perform destructive testing on defueled cladding. To support this activity, equipment has been fabricated to perform this task and a process developed to remove the fuel and decontaminate it sufficiently to work with the samples outside of the hot cells.

Section 3.1 describes a system for the dissolution of fuel from 10 fuel rods delivered to the hot cells in the High-Level Radiochemistry Facility (HLRF) at the PNNL Radiochemical Processing Laboratory (see Shimskey et al. 2019). This fuel dissolution system has been designed, fabricated, and cold tested. However, because of the limited room in the hot cells, the dissolution system has not yet been installed pending completion of the gas communication testing (described in Section 2).

Section 3.2 describes fuel dissolution of two samples cut from rod 6U3L08 (UL-3-1, 5.98-in. length) and from rod F35K13 (FK-4-1, 3.36-in. length) shown in Table 3-1, along with resulting analytical and dose measurements of the cladding.

Table 3-1. Dissolution Testing Sample Description

Sample ID	Source Assembly/Rod Identification	Clad Type	~ Rod-Average Burnup (GWd/MTU)	Cooling Time[a] (yr)	Sample Length	Location from Bottom of Rod
UL-3-1	6U3L08	ZIRLO®	55	12.2	152 mm	926-1078 mm
FK-4-1	F35/K13	Zry-4	59	30.3	85 mm	15 – 100 mm

a) As of June 2019

3.1 Dissolution Apparatus

A fuel dissolution system was designed and fabricated as depicted in Figure 3-1 through Figure 3-3. The system is comprised of a ~1-liter dissolution vessel [8.5 in. x 3.65 in. x 4.0 in., width, depth, height (WDH)] machined out of 304L stainless steel (SST). Attached to the dissolution vessel are two 8-in. Watlow SGA1J8AO9 400-W strip heaters for elevated temperature dissolution. The temperature controller with over-temperature protection is used to control the temperature during dissolution.

The dissolution vessel is sized to dissolve up to four 6-in. fuel rod samples (or equivalent) in one batch. An SST basket, which holds fuel cladding samples between 0.5- and 6-in. long, is placed inside the dissolution vessel. The basket will hold the fuel samples in specific locations and will maintain their orientation during the dissolution process. Different baskets can be selected based on the sizes of fuel samples. A photograph of one of the baskets is shown in Figure 3-3.

The dissolution vessel is mounted on a scissors jackstand that has approximately 6 in. of vertical travel, and the jackstand is mounted on an SST sliding drawer, which provides approximately 6 in. of horizontal travel. With the jackstand lowered and the drawer slid into the forward position, the basket holding the fuel rods can be placed into the dissolution vessel. Once loaded, the dissolution vessel is slid back to the rear position and the jackstand is raised to come into contact with a 0.25-in.-thick stationary SST plate, which forms a seal during the dissolution process. To the stationary plate is mounted a thermocouple to monitor temperature, a funnel to add reagents, a sonicator to aid in mixing, and two condensers that are cooled with chill water.

Nitric acid is added to the dissolution vessel through the addition funnel; 5.5 M HNO_3 was selected as the acid charge based on work done by Johnson and Stone (1980). At this acid concentration and a solution temperature of 100 °C the corrosion potential of zirconium is 1030 mV/SHE, slightly lower than the redox potential of the nitric acid solution at 1070 mV/SHE (Fauvet 2012). This value is within the passivity region of zirconium. By reducing the dissolution temperature from 100 °C the potential for zirconium corrosion is reduced. This initial acid charge should provide adequate excess nitric acid to prevent the formation of insoluble plutonium products. The dissolution follows these formulas:

$$UO_2 + 2.7\ HNO_3 \rightarrow UO_2(NO_3)_2 + 0.7\ NO + 1.35\ H_2O \tag{3-1}$$

$$UO_2 + 4\ HNO_3 \rightarrow UO_2(NO_3)_2 + 2\ NO_2 + 2\ H_2O \tag{3-2}$$

Where reaction 3-1 occurs predominantly at lower acid concentrations and reaction 3-2 occurs at acid concentrations greater than 8 M.

The dissolution vessel is maintained under slight vacuum (via an air operated venturi vacuum system) and off-gas (calculated to not exceed 1 liter/min) is drawn from the dissolution vessel through the off-gas system to reduce the acid vapors in the hot cell. The off-gas system is composed of a condenser, condensate knockout pot, NaOH scrub, and silica gel to adsorb NO_2.

When dissolution is completed, the dissolved fuel is drained from the dissolution vessel directly into a 1-liter SST container (Eagle Stainless Model BTB-10 316L SS 1L) for safe storage prior to disposal. The fuel cladding may undergo additional cleanup steps to help remove fuel residue and reduce cladding dose. The proposed steps include a leaching step with 10 M HNO_3 and a rinse step with 1 M HNO_3. Both of these steps would take place with sonication.

The final rinse step will take place in a clean basket and glass cylinder that have never been exposed to concentrated dissolution or leach solution. A photograph of this basket and graduated cylinder is shown in Figure 3-4. Ideally, the dissolution, leach, and rinse step would occur as a counter-current batch process as indicated in Figure 3-5. Such a process will help minimize liquid waste volume in the hot cell while producing clean cladding.

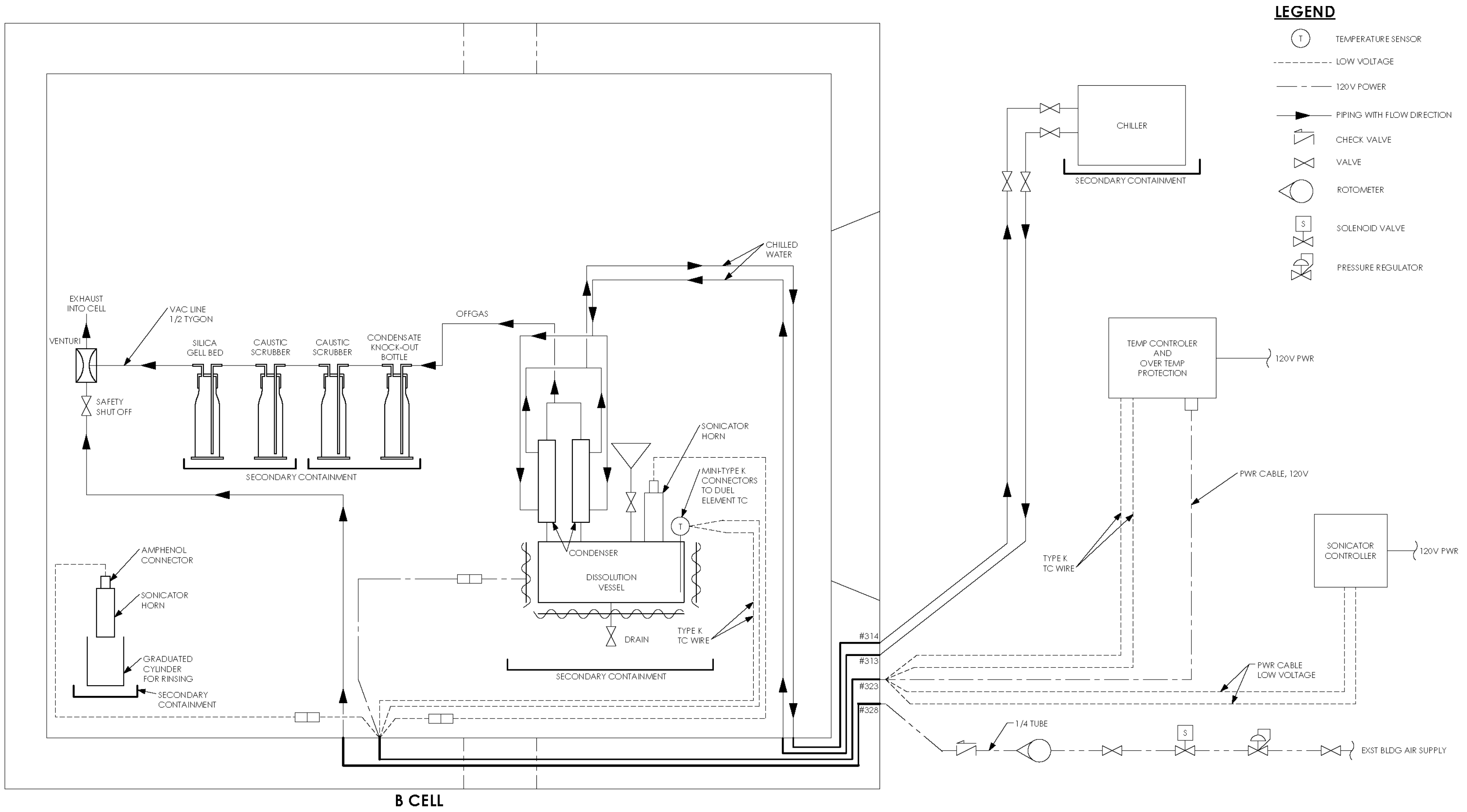

Figure 3-1. Simplified Dissolution System P&ID

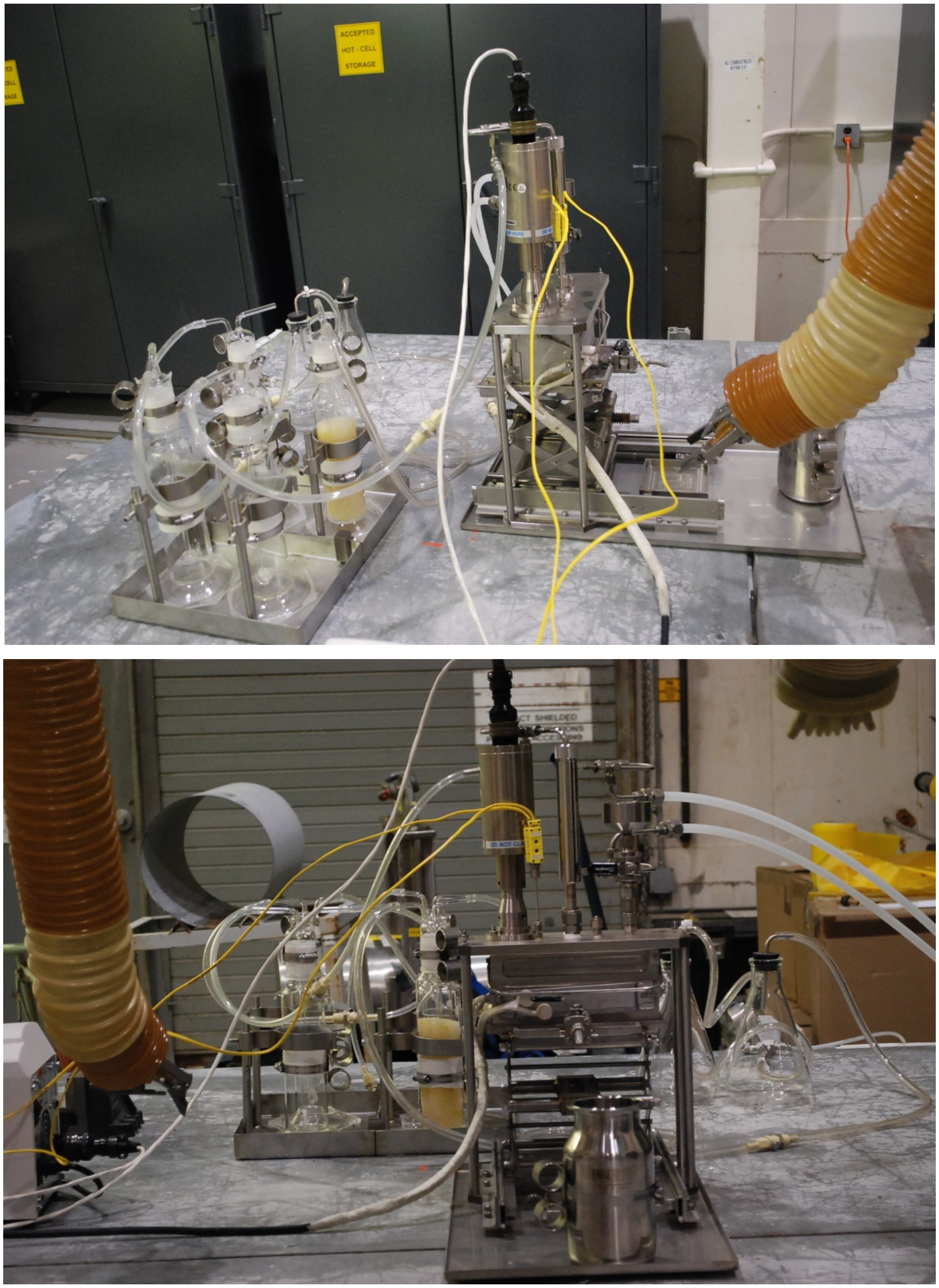

Figure 3-2. Photos of Dissolution System: (top) Front View and (bottom) Side View

Figure 3-3. Dissolution Basket.

Figure Notes: Samples 0.5 in. Long Are Placed Vertically in the 12 Available Cylindrical Slots. Longer samples are placed horizontally (10-degree incline) and there are four available positions. Tubing (3/8-in. diameter x 6-in. long) is shown in one of the horizontal positions.

Figure 3-4. Rinse Basket and Rinse Cylinder

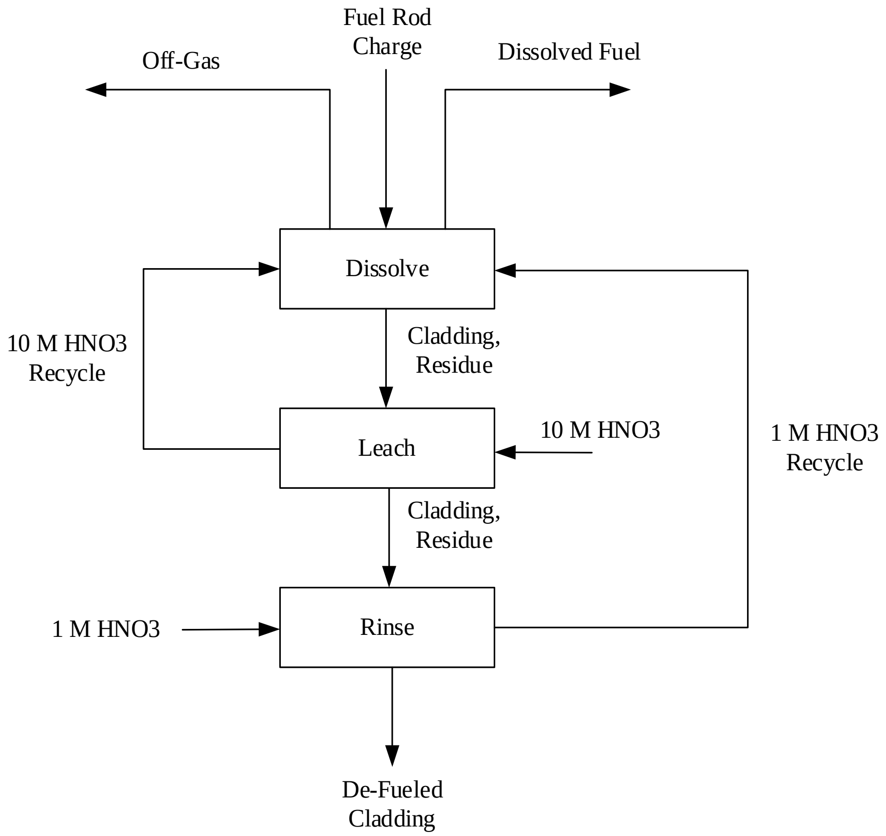

Figure 3-5. Batch Dissolution Flowsheet

3.2 Test Dissolution

A dose profile of de-fueled cladding was desired for estimating personnel dose while handling irradiated cladding samples in future work outside of the hot cells. To obtain this dose profile, a test dissolution system was fabricated, and two sections of fuel rod were selected for dissolution. Moreover, concerns were raised regarding the stresses the 6-in. cladding samples would encounter should these lengths of fuel be drilled to remove the center core of the fuel. Therefore, the test dissolution also established the feasibility of fuel dissolution without pre-drilling.

Table 3-2 summarizes the conditions used to dissolve the fuel from the UL-3-1 and FK-4-1 samples. Shimskey et al. (2019) details the specifics of these samples. All reagents used were ACS grade and diluted with 18 Megohm deionized water. The larger volume of acid used was to ensure the fuel samples remained fully submerged while in a vertical position within the dissolution vessel. Temperature set points were varied to determine if the dissolution kinetics of a lower set-point would satisfactorily remove the fuel in 1 day. This lower temperature set-point would be advantageous for material longevity.

Table 3-2. Dissolution Conditions

Assembly/Rod ID	6U3L08	F35K13
Sample ID	UL-3-1	FK-4-1
Location of the Bottom of Sample from the Bottom of the Rod (mm)	926	15
Sample Length (mm)	152	85
Total Charge (g) (clad + fuel)	98.42	54.87
Oxide Fuel Charge (g)	82.47	45.79
Initial Acid Charge (M)	5.5	5.5
Initial Acid Volume (mL)	1250	1000
Total Dissolving Time (hr)	25.2	24.2
Total Time at Temperature (hr)	11.7	12.3
Solution Temperature Set-point (°C)	85	60
Heating Rate (°C/min)	1.0	0.8

The test dissolution system (Figure 3-6) consisted of a hotplate installed in the HLRF B-Cell and a SST container of the same type that will be used to store the dissolved fuel in the larger scale dissolver, an Eagle Stainless Model BTB-10 316L SST 1L container. The fuel sample was placed in a SST wire basket and lowered into the SST container containing 5.5 M HNO_3 (see Figure 3-7).

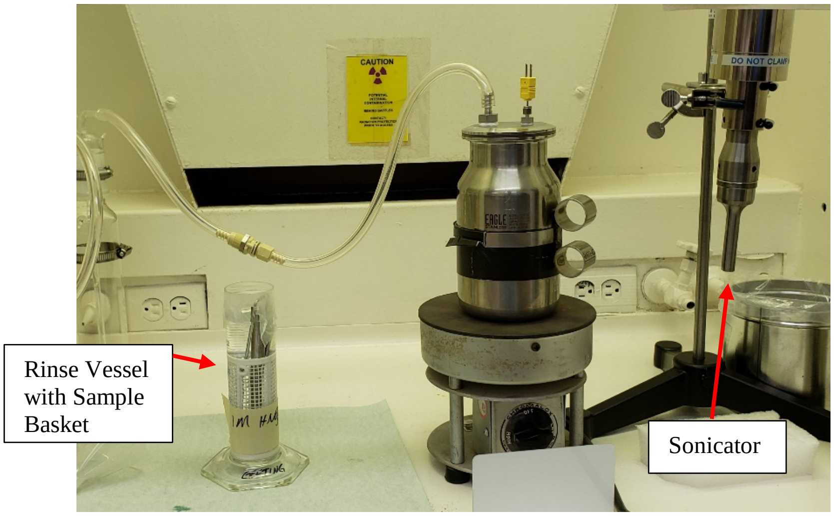

Figure 3-6. Test Dissolution System

The hot plate was controlled with a type-K thermocouple immersed in the dissolution solution and a PID (proportional–integral–derivative) temperature controller located in the operating gallery. Intermittently, the lid was taken off of the dissolution vessel, the SST basket with the clad sample was removed, and the progress of fuel dissolution was measured with a depth gauge. After visual confirmation that all of the fuel had been dissolved out of the cladding (Figure 3-8), the cladding was leached with 10 M HNO_3. In previous fuel dissolution testing, 10 M HNO_3 has been successfully used to remove Pu and ^{106}Ru that may have been insoluble at dissolver acid concentrations (Johnson and Stone 1980). A cut-down 500-mL glass graduated cylinder was used as the leach vessel. This vessel was used after dissolution by transferring the

SST wire basket holding the de-fueled cladding from the dissolution vessel and washed with 0.1 M NaOH from a squeeze bottle, and then the basket was lowered into the leach vessel.

A sonicator (Branson Ultrasonics SFX550 Sonifier® Cell Disruptor, with 0.5-in. Tapped Disruptor Horn) was then placed into the leach vessel. The horn was positioned 0.5 in. above the top of the cladding sample (see Figure 3-9). A sonication program was initiated as described in the summary list below. After leaching, the sample was again washed with 0.1 M NaOH, weighed, and transferred to a poly-coated wire basket. This basket was then placed in the rinse vessel. As before, this was a cut-down glass graduated cylinder. This vessel was placed under the sonicator and the sonication program was initiated.

Sonication/Rinse & Leach Summary:

- Leach of UL-3-1 sample: 5 seconds on, 30 seconds off, using a 33% amplitude, 5.6 min of sonication time, Flipped sample then used same settings for 5.1 min in ~325 mL of 10M HNO_3.
- Rinse of UL-3-1 sample: 5 seconds on, 30 seconds off, using a 33% amplitude, 5.9 min sonication time, flipped sample then used same settings for 5.7 min in ~325 mL 1M HNO_3.
- Leach of FK-4-1 sample: 5 seconds on, 30 seconds off, using a 33% amplitude, 16 min of sonication time in ~325 mL of 10 M HNO_3. Sample was not flipped
- Rinse of FK-4-1 sample: 5 seconds on, 30 seconds off, using a 33% amplitude, 8.25 min of sonication time in ~325 mL 1 M HNO_3. Sample was not flipped.

After the rinse step was completed the cladding samples were again washed with 0.1 M NaOH to neutralize any remaining acid.

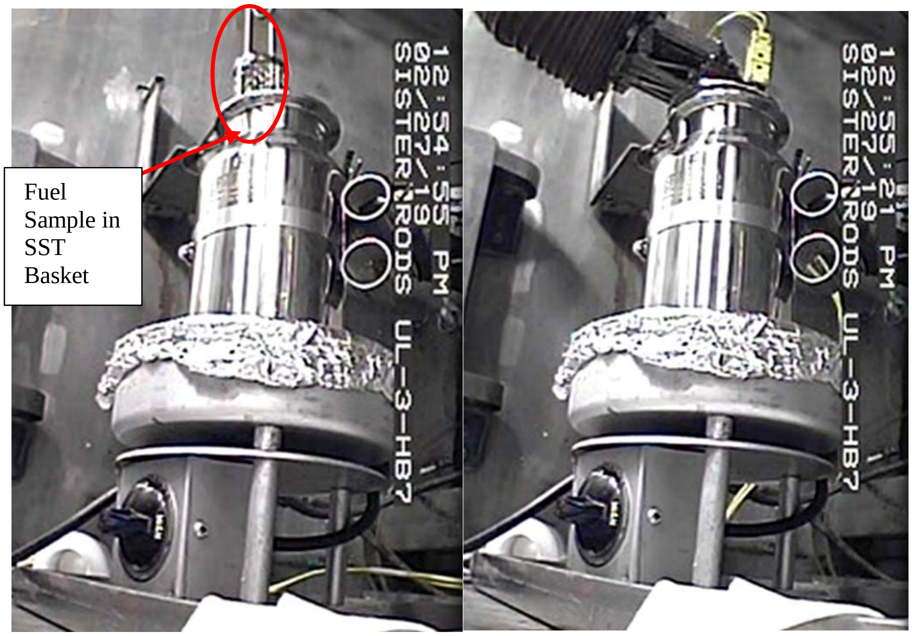

Figure 3-7. Test Dissolution of Sample FK-4-1

Figure 3-8. De-fueled Sample UL-3-1

Figure 3-9. Leached and Cleaned Sample UL-3-1

3.2.1 Results

The dissolution rate for sample UL-3-1 was monitored by depth gauge checks and the results are summarized in Table 3-3. In this sample, fuel dissolved much quicker out of the top end of the sample. After each depth gauge check, the sample was flipped on end to optimize dissolution.

Table 3-3. Sample UL-3-1 Depth Gauge Checks

Dissolution Time (hr)	Top Depth (in.)	Bottom Depth (in.)	Top Δ Depth (in.)	Bottom Δ Depth (in.)
3.65	2.25	0.25	2.25	0.25
18.70	3	2.25	2.75	0
25.48	FDO	FDO	-	-

FDO = Fuel Dissolved Out

Sample FK-4-1 displayed the opposite trend, with fuel dissolving faster out of the bottom end of the sample as shown in Table 3-4. Both samples were left unheated overnight in the dissolution solution. Sample UL-3-1 was checked the morning after at the 18.7-hr dissolution time point, while sample FK-4-1 was checked in the morning at the 24.38-hr dissolution time point.

Table 3-4. Sample FK-4-1 Depth Gauge Checks

Dissolution Time (hr)	Top Depth (in.)	Bottom Depth (in.)	Top Δ Depth (in.)	Bottom Δ Depth (in.)
3.08	0	0.375	0	0.375
5.95	0.375	1.625	0	1.625
24.38	FDO	FDO	-	-

FDO = Fuel Dissolved Out

The cladding samples were weighed after each process step. This included post dissolution, post leach, and post rinse; these values are provided in Table 3-5 and Table 3-6. As expected, the leach removed insoluble solids that were adhered to the cladding.

Table 3-5. Test Dissolution Samples (post-dissolution, before leach)

Sample ID	Sample Mass (g) (clad)	Mass of Fuel Removed (g)	Specific Mass Removed (g/in.)
UL-3-1	15.95	82.47	13.79
FK-4-1	9.08	45.79	13.63

Table 3-6. Mass Removal from Cleaning Process

Sample ID	Mass Removed During Leach (g)	Mass Removed During Rinse (g)
UL-3-1	0.05	0
FK-4-1	0.03	0.16*

*Determined sample was not fully dried.

3.2.2 ICP-MS Results

An aliquot of the dissolved fuel solution was taken for inductively coupled plasma mass spectrometry (ICP-MS) measurement to analyze for rare earth elements, actinides, and quantify uranium enrichment. These results are shown in Table 3-7 and Table 3-8, nuclide identification was based on an ORIGEN run that used the average rod burnup and supplied cooling times to determine isotope generation and depletion. ^{239}Pu was the predominant non-uranium actinide present and ^{139}La was the predominant rare earth element.

Table 3-7. Rare Earth and Actinide ICP-MS Results

Analyte	Nuclide	UL-3-1 Fuel Sample (ng/in.)	FK-4-1 Fuel Sample (ng/in.)
139 m/z	La-139	3.20E+05	1.65E+05
140 m/z	Ce-140	3.11E+05	1.59E+05
141 m/z	Pr-141	2.77E+05	1.45E+05
146 m/z	Nd-146	1.75E+05	8.21E+04
149 m/z	Sm-149	4.38E+02	3.44E+02
154 m/z	Sm-154, Eu-154, Gd-154	1.55E+04	5.83E+03
237 m/z	U-237, Np-237, Pu-237	1.04E+05	4.59E+04
239 m/z	Pu-239	8.84E+05	7.83E+05
240 m/z	Pu-240	4.50E+05	2.81E+05
241 m/z	Pu-241, Am-241	2.82E+05	1.58E+05

Table 3-8. Uranium Enrichment ICP-MS Results

Analyte	UL-3-1 Fuel Sample (ng/in.)	FK-4-1 Fuel Sample (ng/in.)
U-235	1.00E+06	1.99E+06
U-238	1.38E+08	1.42E+08
% U-235	0.73%	1.38%
Initial Enrichment (% U-235)	4.45%	3.59%
~Rod-Average Burnup (GWd/MTU)	55	58

3.2.3 Smear Gamma Energy Analysis (GEA) Results

Results for gamma activity detected on cotton swab smears taken from the cladding samples are shown in Table 3-9, Table 3-10, and Table 3-11. Smears were taken first on the outside diameter of the cladding sample, these are labeled with “Cladding”. Next smears were taken of the top and bottom inside diameter of each sample, denoted with “T-Smear” and “B-Smear,” respectively. The blank smear results are given in Table 3-11.

Table 3-9. Sample UL-3-1 Smear GEA Results

Sample ID	UL-3-1 Cladding		UL-3-1-T-Smear		UL-3-1-B-Smear	
Isotope	**Activity (Bq ± 1 s rel unc)**		**Activity (Bq ± 1 s rel unc)**		**Activity (Bq ± 1 s rel unc)**	
Mn-54	-	-	2.59E-01	60%	-	-
Co-60	2.72E+06	2%	1.01E+01	2%	1.18E+01	2%
Nb-94	6.85E+06	1%	-	-	-	-
Sb-125	3.46E+07	2%	1.33E+02	2%	1.83E+02	2%
Cs-134	1.33E+07	2%	1.08E+02	2%	2.05E+02	2%
Cs-137	3.16E+08	2%	3.78E+03	2%	4.28E+03	2%
Eu-154	9.50E+06	2%	1.18E+02	2%	8.48E+01	2%
Eu-155	1.70E+06	14%	3.91E+01	2%	2.22E+01	2%
Am-241	-	-	4.84E+01	2%	3.56E+01	2%

Table 3-10. Sample FK-4-1 Smear GEA Results

Sample ID	FK-4-1 Cladding		FK-4-1-T-Smear		FK-4-1-B-Smear	
Isotope	**Activity (Bq ± 1 s rel unc)**		**Activity (Bq ± 1 s rel unc)**		**Activity (Bq ± 1 s rel unc)**	
Mn-54	-	-	2.00E-01	26%	-	-
Co-60	4.00E+05	2%	2.94E+00	2%	3.14E+00	2%
Nb-94	-	-	-	-	-	-
Sb-125	3.18E+05	7%	5.59E+00	5%	4.16E+00	7%
Cs-134	7.39E+03	23%	9.66E-01	8%	9.56E-01	9%
Cs-137	9.90E+07	2%	4.04E+03	2%	7.30E+03	2%
Eu-154	8.16E+05	2%	4.60E+01	2%	6.03E+01	2%
Eu-155	7.90E+04	48%	4.16E+00	6%	6.81E+00	12%
Am-241	-	-	1.79E+02	1%	2.76E+02	3%

Table 3-11. Blank Smear GEA Results

Sample ID	Blank-Smear	
Isotope	Activity (Bq ± 1 s rel unc)	
Mn-54	3.28E-01	11%
Co-60	1.42E+01	2%
Nb-94	-	-
Sb-125	3.82E+01	2%
Cs-134	3.68E+00	2%
Cs-137	1.00E+02	2%
Eu-154	1.48E+00	2%
Eu-155	3.90E-01	2%
Am-241	1.47E+00	2%

3.2.4 Dose Measurements

In order to develop an estimated dose to workers while handling irradiated cladding samples outside of the hot cells, multiple measurements were taken. Dose measurements were taken at 1 in., 8 in., and 1 ft from the side and end of each de-fueled cladding sample with a Thermo Scientific Model RO-20 Ion Chamber Survey Meter (see Figure 3-10). Measurements were repeated with the beta window closed and then open to determine the beta radiation contribution to total dose. Results from this survey are given in Table 3-12 and Table 3-13.

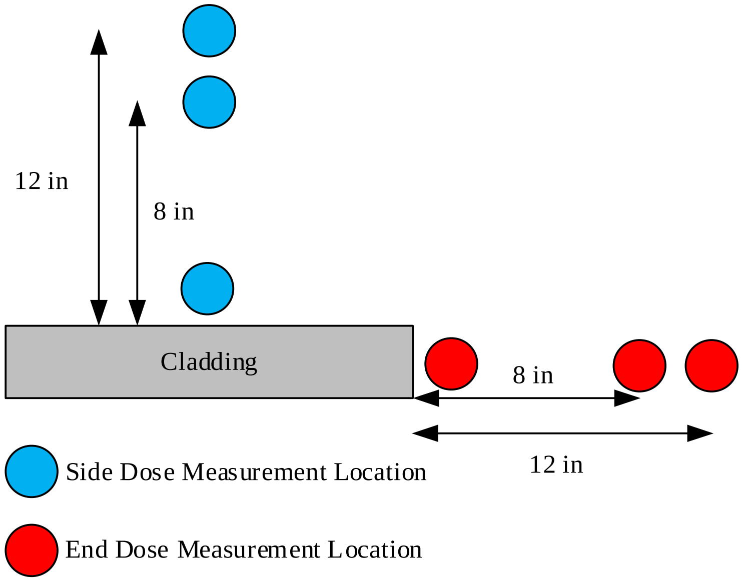

Figure 3-10. Dose Measurement Location Diagram

Table 3-12. Measured Dose Rates for Sample UL-3-1

		End			Side		
	Distance	Open Window (mR/hr)	Closed Window (mR/hr)	Beta Contribution (mR/hr)	Open Window (mR/hr)	Closed Window (mR/hr)	Beta Contribution (mR/hr)
After 1 M HNO_3 Rinse	1 ft	350	80	270	800	80	720
	8 in	2500	100	2400	1500	150	1350
	1 in	>50000	1200	>50000	12000	2000	10000
After 10 M HNO_3 Leach	1 ft	1000	80	920	800	100	700
	8 in	2500	120	2380	1000	150	850
	1 in	>50000	1000	>50000	10000	2000	8000
After Dissolution Only	1 ft	-	-	-	1000	100	900
	8 in	-	-	-	2000	300	1700
	1 in	-	-	-	15000	2000	13000

Table 3-13. Measured Dose Rates for Sample FK-4-1

		End			Side		
	Distance	Open Window (mR/hr)	Closed Window (mR/hr)	Beta Contribution (mR/hr)	Open Window (mR/hr)	Closed Window (mR/hr)	Beta Contribution (mR/hr)
After 1 M HNO_3 Rinse	1 ft	400	8	392	150	8	142
	8 in	1000	15	985	300	20	280
	1 in	10000	100	9900	2800	200	2600
After 10 M HNO_3 Leach	1 ft	200	8	192	100	8	92
	8 in	500	100	400	200	15	185
	1 in	12000	150	11850	5000	350	4650
After Dissolution Only	1 ft	250	5	245	100	8	92
	8 in	500	12	488	200	15	185
	1 in	15000	100	14900	2500	180	2320

The effectiveness of the leach and rinse steps at reducing dose are quantified[o] as decontamination factors (DFs) given by:

$$DF = \frac{D_{before}}{D_{after}} \tag{3-6}$$

Where D_{before} is the measured dose before the process step and D_{after} is the measured dose after the process step. Higher values denote more effective decontamination. These DF values are provided in Table 3-14 and Table 3-15. On average the leach step was better at reducing open window dose while the rinse step on average reduced the closed window dose more effectively.

---

[o] It must be acknowledged that the dose measurements were taken by different personnel and distances were estimated. Based on observation during the dose measurements, the listed distances have a likely uncertainty of +/-30%.

Table 3-14. Decontamination Factors for Sample UL-3-1

		End		Side	
	Distance	**Open Window DF**	**Closed Window DF**	**Open Window DF**	**Closed Window DF**
After 1 M HNO_3 Rinse	1 ft	2.86	1.00	1.00	1.25
	8 in.	1.00	1.20	0.67	1.00
	1 in.	-	0.83	0.83	1.00
After 10 M HNO_3 Leach	1 ft	-	-	1.25	1.00
	8 in.	-	-	2.00	2.00
	1 in.	-	-	1.50	1.00

*Shaded boxes indicate DF < 1.

Table 3-15. Decontamination Factors for Sample FK-4-1

		End		Side	
	Distance	**Open Window DF**	**Closed Window DF**	**Open Window DF**	**Closed Window DF**
After 1 M HNO_3 Rinse	1 ft	0.50	1.00	0.67	1.00
	8 in.	0.50	6.67	0.67	0.75
	1 in.	1.20	1.50	1.79	1.75
After 10 M HNO_3 Leach	1 ft	1.25	0.63	1.00	1.00
	8 in.	1.00	0.12	1.00	1.00
	1 in.	1.25	0.67	0.50	0.51

*Shaded boxes indicate DF < 1.

This page intentionally left blank

4. BURST SYSTEM

One of the mechanical destructive tests outlined in Saltzstein et al. 2018 to be performed on defueled cladding is a burst test performed under ASTM B811-03 (ASTM 2013) to compare hoop stress/strain properties at different temperatures and with axial stress/strain properties measured from tensile tests. This section describes the equipment developed to perform this test at room temperature as well as 200°C with 6 in. defueled cladding samples

4.1 Burst System Apparatus

A system to conduct burst testing on Zircaloy nuclear grade cladding at pressures up to 20,000 psi and temperatures up to 200°C was designed and fabricated as depicted in Figure 4-1. Shakedown testing of the system and installation in the Radiochemical Processing Laboratory to allow testing of radioactive test articles are pending.

Planned testing is conducted by filling the system tubing with water and removing residual air out of the system and cladding specimen. When heating the system for an elevated temperature test, pressure will increase due to thermal expansion of the water, but a relief valve will keep the pressure below 500 psig.[p] Once the heating phase and thermal expansion are complete, the relief valve is isolated and the system is pressurized in a controlled manner (in accordance with Annex A.1 of ASTM B811-03 [ASTM 2103]) until the test article bursts.

Components of the burst system are rated for 20,000 psi or higher. The test article will fail in the 10,000-18,000 psi range. When testing is conducted at room temperature, a small amount of water will be released from the test article to the oven (~34 mL). When testing is conducted at elevated temperature, a water/steam mixture will be released. Energy is dissipated rapidly upon cladding rupture due to the low compressibility of water and the small volume of steam produced.

A video image system will take pictures of the cladding during testing to produce synchronized stress-strain curves. The test article will be contained inside an oven that will control the temperature and provide shielding from the burst. Additionally, the oven will be placed inside a fumehood to ensure the control of any contamination.

Key features include the following:

- A positive displacement piston pump is used to fill the system with water. When all the air has been displaced from the system, the pump and water reservoir are isolated from the high-pressure portion of the burst system.
- Piston screw pumps to generate high pressure. Each pump can provide 10-mL volume into the system at pressures up to 60,000 psi. A pressure gauge is on the table with the pumps so that the operator can control and monitor the pressure during testing. A photograph of the pumps set upon a table is provided in Figure 4-2.
- A pressure relief valve (set at 500 psi) in the fume hood prevents the system from over-pressurization during heating. The pressure relief valve is isolated from the system during the final pressurization and bursting of the test article.
- A pressure-transducer-to-data-acquisition system to provide time correlated stress measurements.
- A digital image correlation system is used, consisting of cameras, image correlation software, and computer for gathering of 3-D strain measurements.

---

[p] Water at 200°C requires pressure greater than ~215 psig to stay in liquid form.

- A custom-built convection oven equipped with internal lights, viewing ports for the camera system, and thermocouple is used to control and maintain the burst system temperature (see Figure 4-3). The oven is 12-in. x 12-in. x 30-in. (WDH) and is fully contained within the fumehood.
- A sintered metal filter is installed in-line at the oven entrance in order minimize thermal convection currents
- A thermocouple inserted into thermal well is used to measure the fluid temperature.
- Airmo model MPG series test tools are used to grip and seal both ends of the test article. The o-rings in the grips were replaced with Parker E0962-90 geothermal EDPM o-rings designed for high temperatures (up to 260°C) and compatible with water/steam. These seals last for approximately 12 bursts cycles at 200°C before replacement is required.
- Fume hood is used for containing and controlling any contamination resulting from the burst tests.
- Supplemental exhaust may be provided if needed to control contamination resulting from the burst process.

All of the key elements of the system have been operationally tested including conducting 12 bursts at elevated temperature, measuring synchronous stress-strain during bursts, and operation of the piston screw pumps. However, the integrated system for testing radioactive test articles inside a contamination area has not yet been tested. Such testing will require generation of a radioactive work permit and may require some modifications of the procedure in order to protect staff and comply with as low as reasonably achievable requirements.

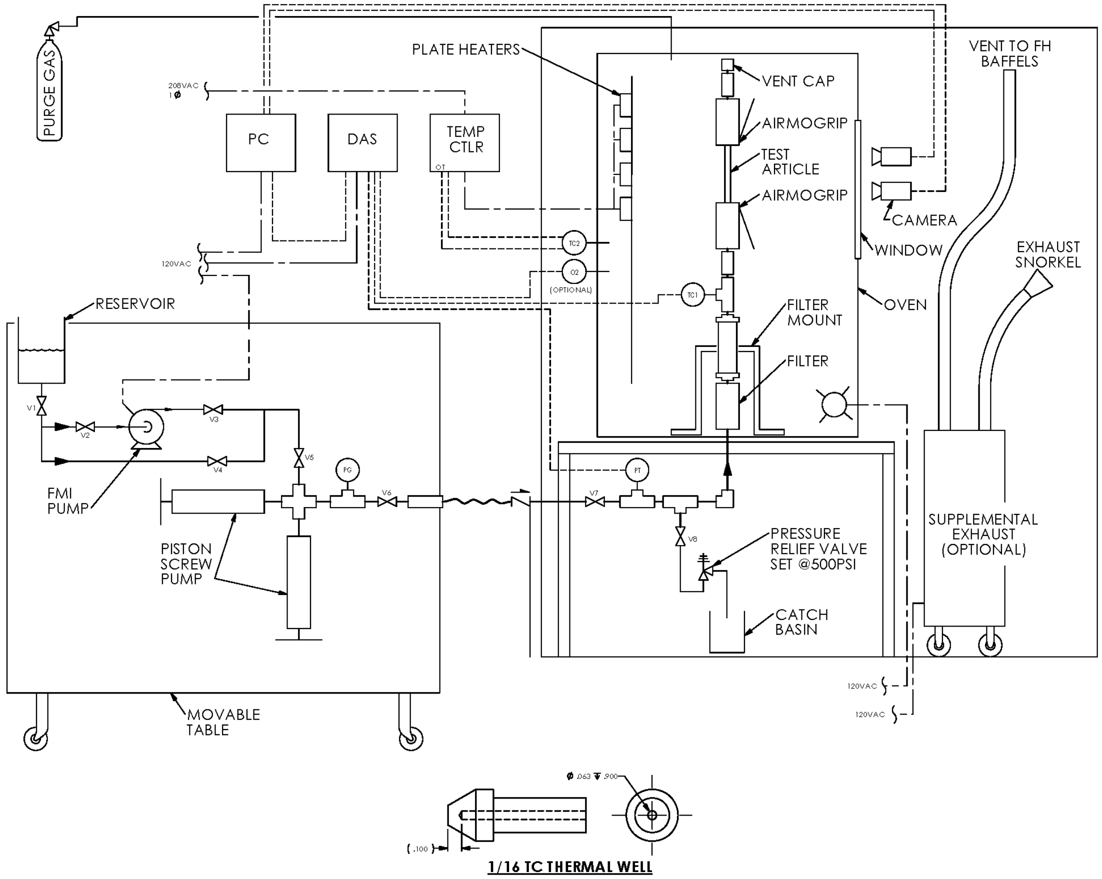

Figure 4-1. Burst System Schematic

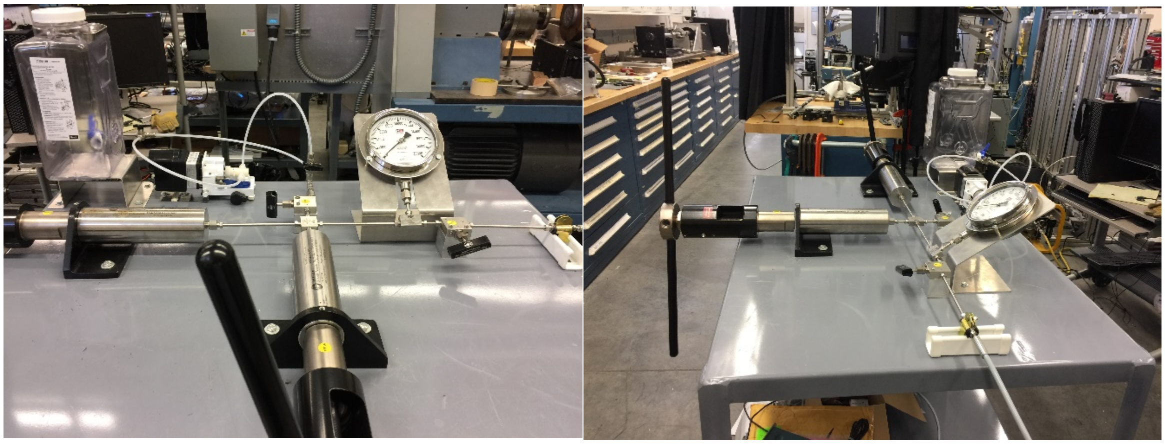

Figure 4-2. Equipment Located on Movable Table

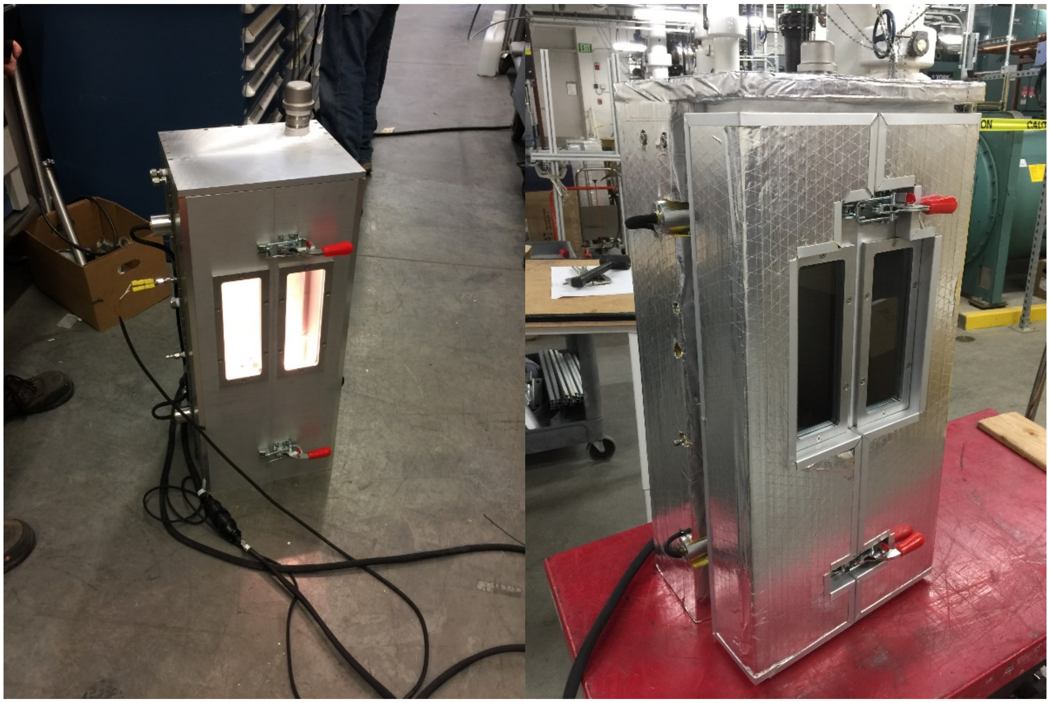

Figure 4-3. Custom Oven Before and After Insulating

5. METALLURGICAL TESTING

Optical metallurgical inspection and microhardness testing is performed to examine the effects of irradiation on nuclear grade Zircaloy cladding. Optical microscopy is used to inspect hydride formation in the cladding. The hardness of the cladding and the Young's Modulus can be determined from microhardness testing. Cold testing is being performed to perfect the sample preparation and examination techniques. Section 5.1 details the work done to prepare the sibling pin samples for these techniques.

To support imaging of hydride formation in the cladding, a LECO analyzer was installed in a radiological ventilated enclosure to provide the hydrogen concentration in the cladding in locations next to where optical microscopy samples are taken. Section 5.2 discusses the operations of the LECO analyzer and its capabilities.

5.1 Metallography Sample Preparation and Examination

5.1.1 Sample Preparation

Sample preparation for both optical examination and microhardness testing use mounted and polished samples. The cladding is cut into 0.25-in. sections using a slow-speed saw (Figure 5-1). The samples are then mounted in an epoxy. Two instruments are used to polish the samples, a Pace Technologies multistage grinder-polisher and a Pace Technologies vibratory polisher (Figure 5-2). The samples are first polished using the multistage polisher using several grits of sand paper, followed by use of polycrystalline diamond suspension. The samples are finished in the vibratory polisher over 12 to 18 hours. This process results in a finely polished specimen that can be seen in Figure 5-3.

5.1.2 Microstructure Examination

Optical microscopy is performed using an Olympus scope (Figure 5-4). The irradiated cladding samples will be examined for hydride formation and orientation. This scope is equipped with 10x and 20x lenses. The scope and the software are capable of image capture and analysis.

Hardness testing is used to identify material characteristics, including tensile strength. In particular, microhardness testing has the advantage of being able to test small samples, which enables us to take multiple measurements in a small region. The Sun-Tec microhardness tester is capable of Vickers and Knoop indentation (Figure 5-5). Figure 5-6 shows five Vickers indentations, made in the radial direction of a cladding sample. These indentations and their measurements are taken at multiple locations on each cladding sample.

Both the optical microscope and hardness tester are calibrated and have the ability to be regularly checked by the user. The scope measurements can be confirmed through the use of a NIST standard reference material microscope magnification standard. The microhardness tested is checked using a certified hardness standard. Both scopes are regularly checked when in operation.

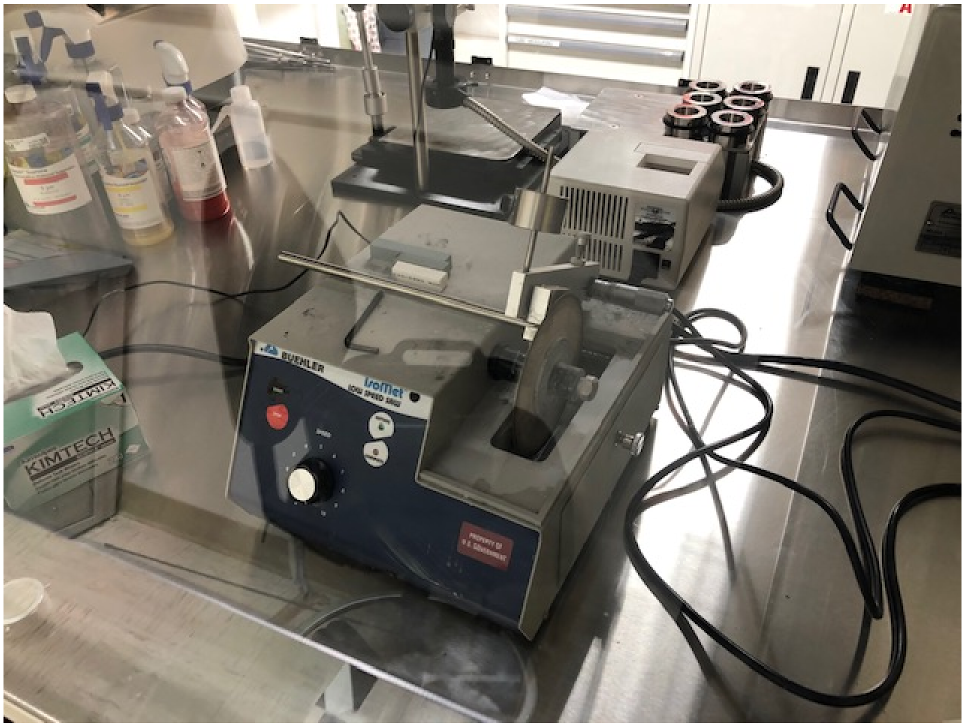

Figure 5-1. Isomet Low-Speed Saw

Figure 5-2. Vibratory Polisher and Multistage Polisher

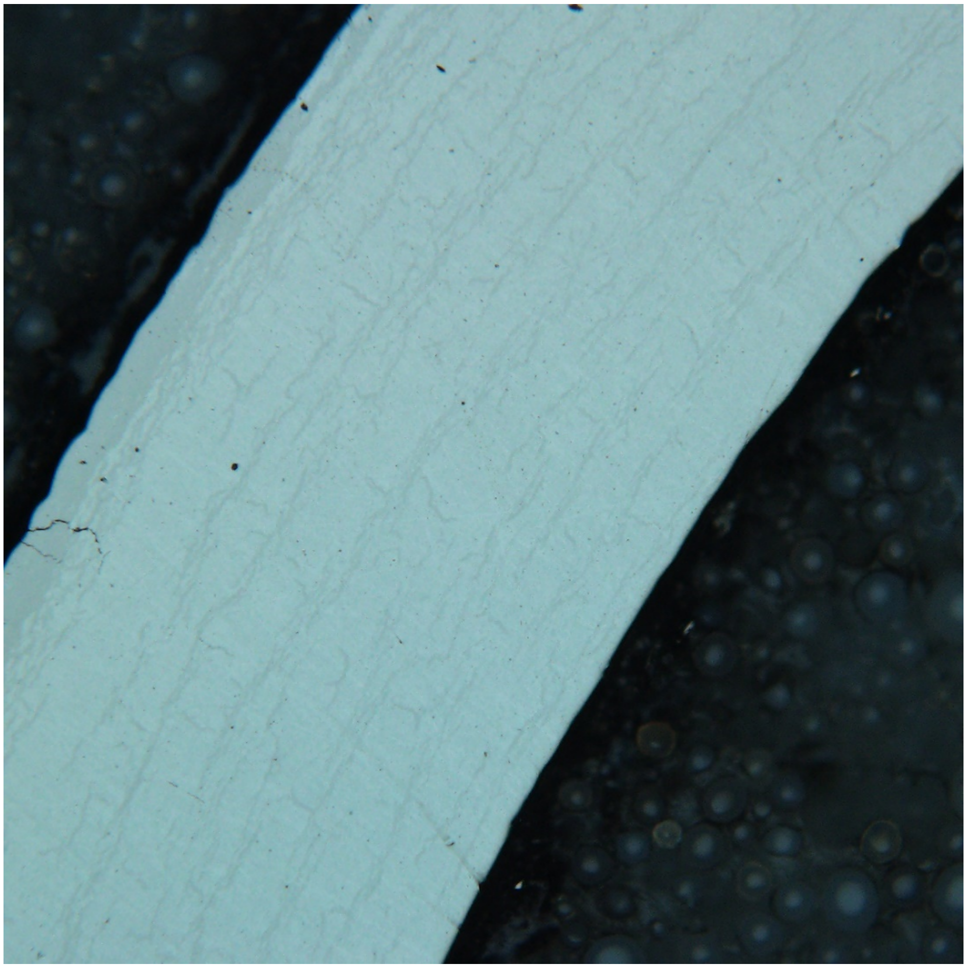

Figure 5-3. Optical Image of Mounted and Polished Non-Irradiated, Pre-hydrided Cladding

Figure Note: Sample is a cross-sectional cut from an as-manufactured 9.5mm diameter cladding sample designed for a 17x17 assembly with a measured wall thickness of 0.60 mm. The sample was hydrided to ~ 500 ppm and heat treated under a hoop stress to create radial hydrides within the wall.

Figure 5-4. Olympus Optical Microscope

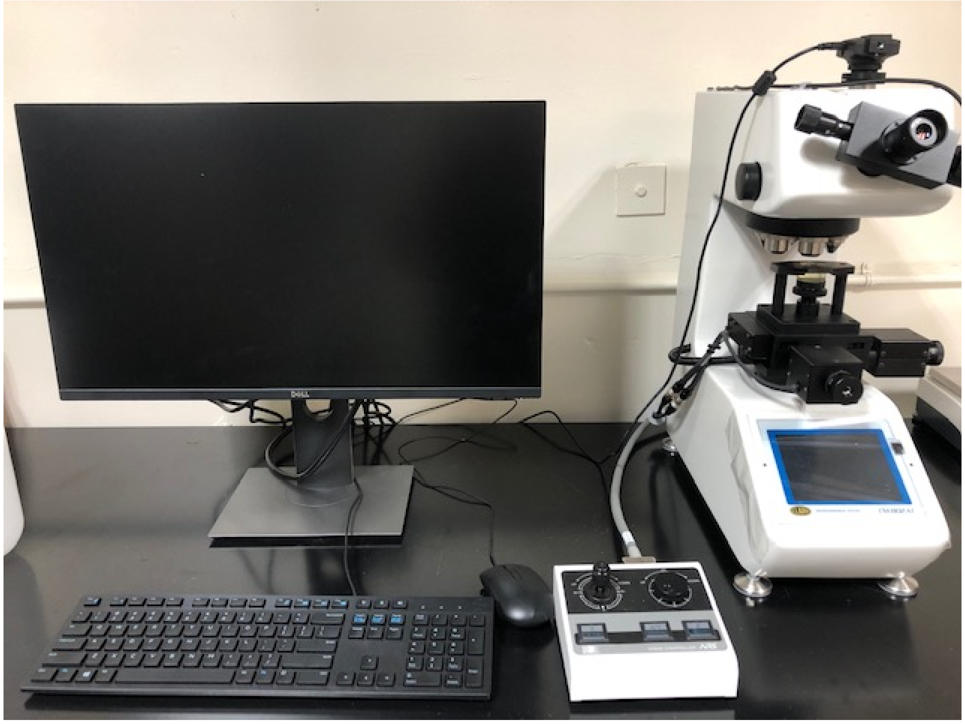

Figure 5-5. Microhardness Tester

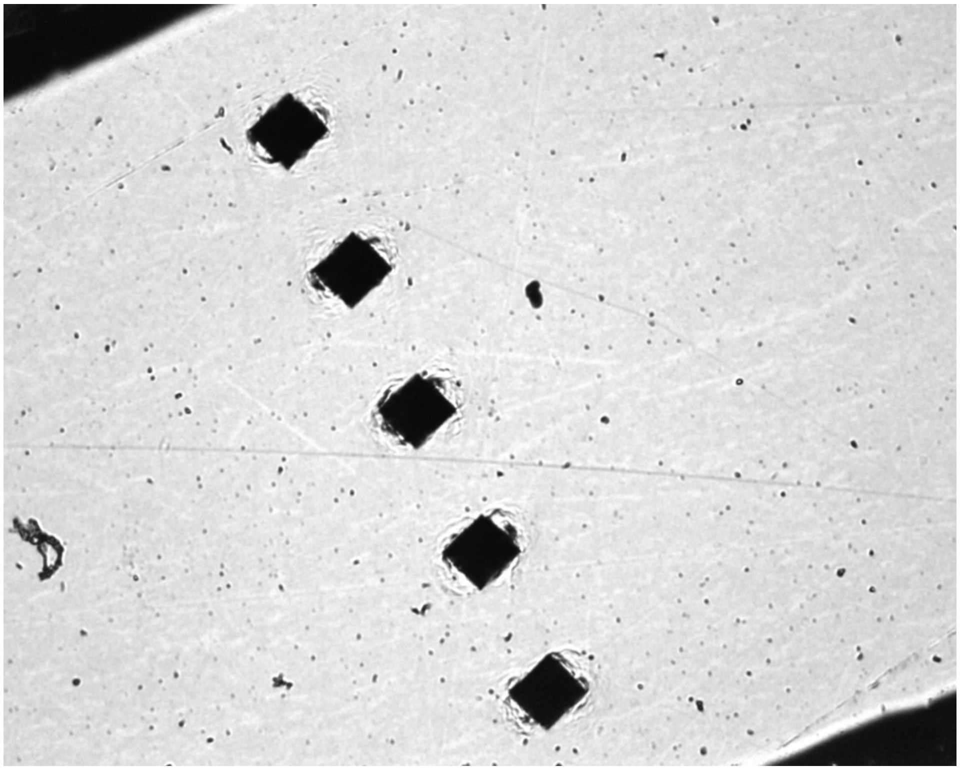

Figure 5-6. Optical Image of Microhardness Indentations

Figure Note: Sample is a cross-sectional cut from an as-manufactured 9.5mm diameter cladding sample designed for a 17x17 assembly with a measured wall thickness of 0.60 mm.

5.2 LECO Measurement of Hydrogen, Oxygen, and Nitrogen in Cladding Samples

The ONH836 Oxygen/Nitrogen/Hydrogen Analyzer is designed for wide-range measurement of oxygen, nitrogen, and hydrogen content of steel, refractory metals, and other inorganic materials. A pre-weighed sample is placed in a graphite crucible, which is heated in an impulse furnace to release analyte gases. An inert gas carrier, helium (He), sweeps the liberated analyte gases out of the furnace, through a mass flow controller, and to a series of detectors. Oxygen present in the sample reacts upon combustion with the graphite crucible to form carbon monoxide (CO) and carbon dioxide (CO_2), which are detected using non-dispersive infrared (NDIR) cells.

Since analyte gas molecules absorb infrared (IR) energy at unique wavelengths within the IR spectrum, incident IR energy at these wavelengths is absorbed as the gases pass through the NDIR absorption cells. The gas continues through a heated copper oxide bed, where CO is oxidized to CO_2 and hydrogen gas (H_2) is oxidized to water (H_2O). The gas then passes through another set of NDIR cells where H_2O and CO_2 are detected. H_2O and CO_2 are then scrubbed out of the carrier gas stream and a dynamic flow compensation system is used to add carrier gas as a makeup for the gas lost during the scrubbing process.

The final component in the flow stream is a thermal conductivity (TC) detector, which is used to detect nitrogen. TC detection takes advantage of the difference in TC between carrier and analyte gases. Resistive TC filaments are placed in a flowing stream of carrier gas and heated by a bridge circuit. As analyte gas is introduced into the carrier stream, the rate at which heat transfers from the filaments will change, producing a measurable deflection in the bridge circuit.

5.2.1 Instrument Modifications

The instrument is designed to sit on a countertop (Figure 5-7a) but was modified to fit into a radioactive fumehood. To fit, it was turned 90° to face the far wall of the fumehood (Figure 5-7b). Covers over reagent tubes were removed from the front of the instrument (Figure 5-7c) and the supplied vacuum was replaced with a high-efficiency particulate air vacuum. For ease of instrument access and a reduction in sample handling time, arm holes were cut into the side of the fumehood (Figure 5-7d).

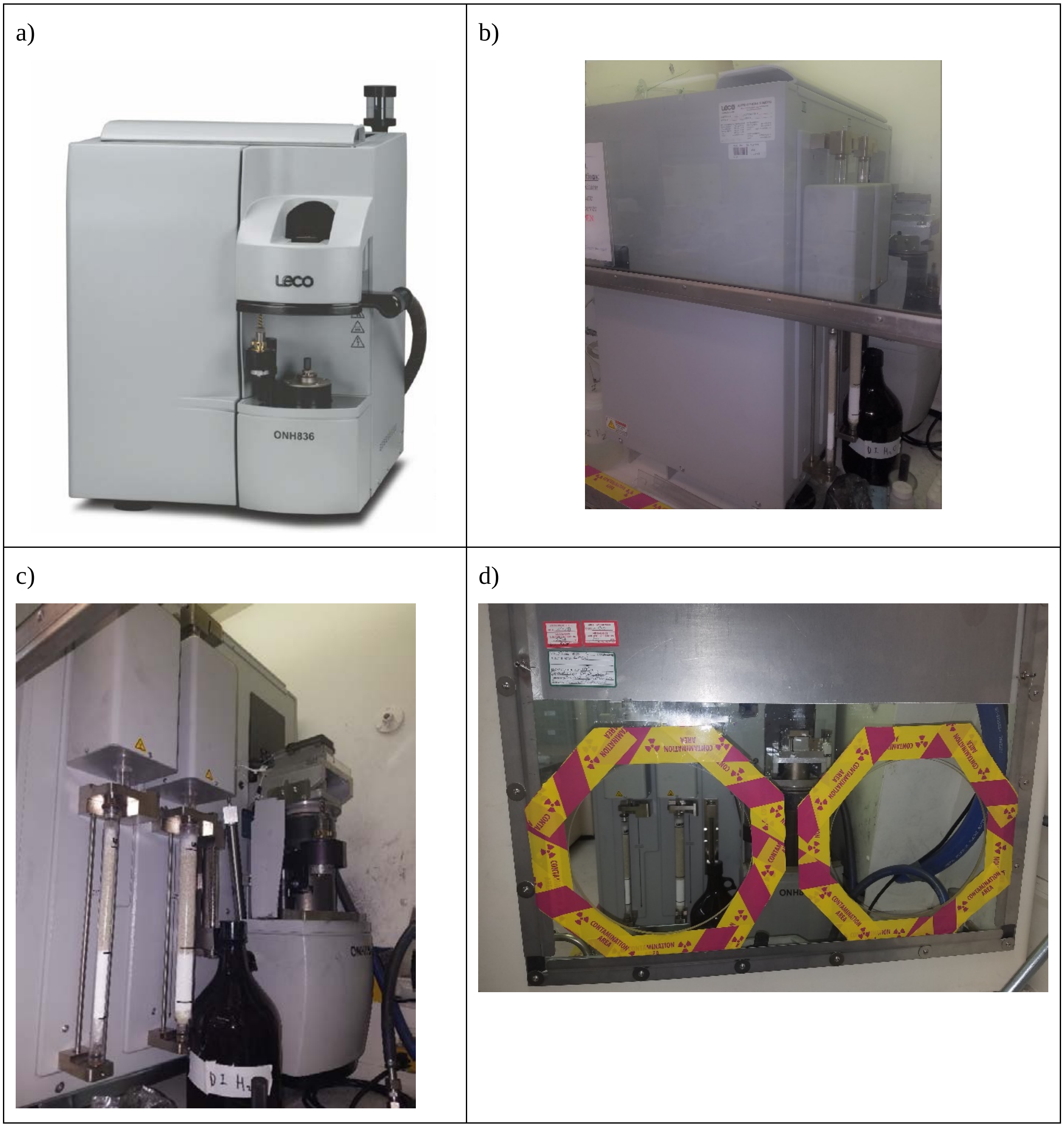

Figure 5-7. a) As Manufactured LECO ONH 836 instrument, b) LECO ONH 836 Fit into Fumehood 90°, c) LECO ONH 836 with Reagent Covers Removed, d) Arm Holes Cut in the Side of the Fumehood

5.2.2 Sample Preparation

Samples are prepared by taking 0.25-in. cladding rings and quartering the rings using an Isomet slow-speed saw (Figure 5-1). Each quarter ring is ~0.05-0.10 g and fits within the ~1-cm^3 LECO crucible and through the LECO sample drop chamber.

This page intentionally left blank

6. SUMMARY

Preliminary gas communication testing performed on the bottom the segment of rod 6U3L08 (segment UL-4, 36 in. length) was compared to the full-length results at ORNL for rod 30AK09, showing similar estimates for hydraulic diameter between 46 to 75 µm. Physical diameter changes of ~ 2 µm for segment UL-4 were measured during testing while pressurized to 5 MPa.

Gas communication testing also took steps to evaluate and quantify particle release during rod depressurization (i.e., during gas communication “decay” testing). Estimates of total release based on ^{134}Cs, ^{137}Cs, and ^{154}Eu activities in this sample final total aerosol fractional release in the range of 10^{-8} to 10^{-7} kg fuel release per kg fuel in rod. In comparison, Hanson et al. (2008) observed fractional releases ranging from 10^{-7} to 10^{-5} for SNF. As such, the fraction released in the current testing seem in line with previous measurements of fuel release.

Dissolution of spent fuel from two spent fuel samples from rod 6U3L08 (sample UL-3-1, 5.98 in. length) and rod F35K13 (sample FK-4-1, 3.36 in. length) also occurred demonstrating that dissolution from samples up to 6 in. length was achievable within a day of operation without drilling. Dose measurements of these defueled cladding samples confirmed that destructive testing of the defueled cladding could occur outside the hot cell.

Development of the burst system for elevated temperature testing is on track as well as the establishment of an optical metallurgical center for cross sectional imaging and microhardness measurements of defueled cladding. The LECO hydrogen analyzer has been operational for the last year and currently running radiological samples in a ventilated enclosure.

This page is intentionally left blank.

7. REFERENCES

ASTM B811-03. 2013. *Standard Specification for Wrought Zirconium Alloy Seamless Tubes for Nuclear Reactor Fuel Cladding*. ASTM International, West Conshohocken, Pennsylvania.

Churchill, S. 1977. "Friction Factor Spans All Fluid-Flow Regimes." *Chemical Engineering* 84(24):91-92.

Coulson, J. and J. Richardson. 1997. C*oulson and Richardson's Chemical Engineering: Volume 1, Fluid Flow, Heat Transfer, and Mass Transfer*, 5th Edition. Butterworth Heinemann, Oxford, United Kingdom.

Dallavalle, J. M. 1948. *Micromeritics: The Technology of Fine Particles.* Pitman Publishing Corp. New York.

Daniel, R.C. and J.C. Berg. 2006. "Spreading on and penetration into thin, permeable print media: Application to ink-jet printing." *Advances in Colloid and Interface Science* 123-126, 439-469.

EPRI (Electric Power Research Institute). 2014. *High Burnup Cask Research and Development Project: Final Test Plan*. Palo Alto, California. February 27, 2014.

Fauvet, P. "Corrosion Issues in Nuclear Fuel Reprocessing Plants." *Nuclear Corrosion Science and Engineering*, 2012, pp. 679–728.

Flynn G.P., R.V. Hanks, N.A. Lemaire, and .J Ross. 1963. "Viscosity of Nitrogen, Helium, Neon, and Argon from -78.5° to 100°C below 200 Atmospheres." *Journal of Chemical Physics* 38: 154-162.

Green, D.W. (Ed.). 1997. *Perry's Chemical Engineers' Handbook*, 7th Edition, McGraw-Hill, New York, New York.

Hanson, B.D., R.C. Daniel, A. Casella, R.S. Wittman, W. Wu, P.J. MacFarlan, and R.W. Shimskey. 2008. *Fuel-In-Air FY07 Summary Report*. PNNL-17275, Rev. 1, Pacific Northwest National Laboratory, Richland, Washington.

Johnson, D.R., and J.A. Stone. 1980. *Light Water Reactor Fuel Reprocessing: Dissolution Studies of Voloxidized and Non-voloxidized Fuel*. Savannah River Laboratory, Aiken, South Carolina. doi:10.2172/711324.

Lemmon, E.W. and R.T. Jacobsen. 2004. "Viscosity and Thermal Conductivity Equations for Nitrogen, Oxygen, Argon, and Air". *International Journal of Thermophysics* 25(1): 21-69.

Montgomery, R., B. Bevard, R.N. Morris, J. Goddard, Jr., S.K. Smith, J. Hu, J. Beale, and B. Yoon. 2018. *Sister Rod Nondestructive Examination Final Report*. SFWD-SFWST-2017-000003, Rev. 1; ORNL/SPR-2017/484, Rev. 1, Oak Ridge National Laboratory, Oak Ridge, Tennessee.

Montgomery, R. and R. Morris. 2019. "Measurement and modeling of the gas permeability of high burnup pressurized water reactor fuel rods." *Journal of Nuclear Materials* 523, 206-215.

Muskat, M. 1934. "Flow of Compressible Fluids Through Porous Media and Some Problems in Heat Conduction." *Physics* 5: 71-94.

Saltzstein, S.J., M. Billone, B. Hanson, and J. Scaglione. 2018. *Visualization of the High-Burnup Spent Fuel Rod Phase 1 Test Plan: Technical Memo*. SAND2018-8042 O, Sandia National Laboratories, Albuquerque, New Mexico.

Shimskey R.W., M.K. Edwards, J. Geeting, J.R. Allred, S.K. Cooley, R.C. Daniel, and R.M. Cox, et al. 2019. *Initial Results of Destructive Examination of Ten Sister Rods at PNNL*. PNNL-28548. Pacific Northwest National Laboratory, Richland, Washington.

Wutz, M., H. Adam, and W. Walcher. 1997. *Handbuch Vakuumtechnik*. Vieweg und Sohn Verlagsgesellschaft. Friedr, Braunschweig.

Appendix A

GAS COMMUNICATION MODEL DEVELOPMENT

The current appendix provides a detailed derivation of the two PNNL equations used to interpret gas transmission pressure evolutions and provide metrics to quantify the rate of gas transmission. To this end, modeling concepts introduced in the main body of the current report are re-introduced herein. However, these concepts are kept more briefly such that the derivation can focus on the individual mathematical steps to reach the final results.

A-1. Conceptual Model

Consider two pressure chambers (chamber 1 and 2), filled with an ideal gas, at time-dependent pressures $P_1(t)$ and $P_2(t)$, respectively, connected by a pipe (or hydraulic channel) of length L and diameter d. If we let $P_1 > P_2$, then gas will flow through the pipe from chamber 1 (termed the upstream chamber) to chamber 2 (termed the downstream chamber). We assume that the upstream and downstream chamber volumes, V_1 and V_2, respectively, are sufficiently large and that gas communication process is sufficiently slow, such that gas transport through the connecting pipe occurs under pseudo-steady-state conditions and that the pipeline inventory of gas is de minimis with respect to the overall gas inventory. The two chamber system is otherwise closed, such that the total moles N of ideal gas is constant. We can write:

$$N = N_1 + N_2 \tag{A-1}$$

where N_1 and N_2 are the number of moles of gas in chamber 1 and chamber 2, respectively. When working in engineering space, it is often easier to work in units of mass. The mass of gas can be evaluated as:

$$m_i = M_w N_i \tag{A-2}$$

Assuming no chemical reactions occur during transport, M_w is fixed for both chambers, so we can related m and N directly. Then,

$$m = m_1 + m_2 \tag{A-3}$$

Here m is the total mass of gas in the two chamber system. Because m is constant,

$$\mathrm{d}m_1 = -\mathrm{d}m_2 \tag{A-4}$$

Next, we consider how mass changes are related to changes in process variables through the ideal gas law (without considering chamber thermodynamics).

A-2. Ideal Gas Law Relations

From the ideal gas law, we can write for chamber i:

$$N_i = \frac{P_i V_i}{R T_i} \tag{A-5}$$

If we define a mass-based gas constant R_m as:

$$R_m = \frac{R}{M_w} \tag{A-6}$$

then the ideal gas law becomes:

$$m_i = \frac{P_i V_i}{R_m T_i} \tag{A-7}$$

The chamber volumes V_1 and V_2 are fixed, such that the total derivate $\mathrm{d}m_i$ can be written in terms of P_i and T_i variation alone:

$$\mathrm{d}m_i = \left(\frac{\partial m_i}{\partial P_i}\right)_{T_i} \mathrm{d}P_i + \left(\frac{\partial m_i}{\partial T_i}\right)_{P_i} \mathrm{d}T_i \tag{A-8}$$

$$= \left(\frac{m_i}{P_i}\right) \mathrm{d}P_i - \left(\frac{m_i}{T_i}\right) \mathrm{d}T_i \tag{A-9}$$

We define a mass flow rate G_i such that

$$G_i = \frac{\mathrm{d}m_i}{\mathrm{d}t} \tag{A-10}$$

where t is time. Thus, the mass flow rate can be related to changes in gas temperature and pressure by:

$$G_i = m_i \left[\frac{1}{P_i} \left(\frac{\mathrm{d}P_i}{\mathrm{d}t} \right) - \frac{1}{T_i} \left(\frac{\mathrm{d}T_i}{\mathrm{d}t} \right) \right] \tag{A-11}$$

Given $G_i(t)$, we can evaluate the $m_i(t)$ as:

$$m_i(t) = m_i^o + \int_0^t G_i(t')\,\mathrm{d}t' \tag{A-12}$$

where m_i^o is the initial mass of gas in chamber i.

A-3. Isothermal Chamber Relationships

Under isothermal conditions at a temperature T, we have a total mass differential $\mathrm{d}m_i$:

$$\mathrm{d}m_i = \left(\frac{m_i}{P_i} \right) \mathrm{d}P_i \tag{A-13}$$

$$= \left(\frac{V_i}{R_m T} \right) \mathrm{d}P_i \tag{A-14}$$

Given the two-chamber relationship $\mathrm{d}m_1 = -\mathrm{d}m_2$, we can write:

$$V_1\,\mathrm{d}P_1 = -V_2\,\mathrm{d}P_2 \tag{A-15}$$

First, we integrate to give:

$$V_1 \left(P_1 - P_1^o \right) = -V_2 \left(P_2 - P_2^o \right) \tag{A-16}$$

where P_1^o and P_2^o are the initial ($t = 0$) pressure for chamber 1 and 2, respectively. Rearrangement gives:

$$V_1 P_1 + V_2 P_2 = V_1 P_1^o + V_2 P_2^o \tag{A-17}$$

The right-hand side of this equation is a constant and holds for any time. In the limit of large time, both P_1 and P_2 approach the same equilibrium pressure P_e such that:

$$\lim_{t \to \infty} V_1 P_1(t) + V_2 P_2(t) = \left(V_1 + V_2 \right) P_e \tag{A-18}$$

Thus,

$$P_e = \left(\frac{V_1}{V_1 + V_2} \right) P_1 + \left(\frac{V_2}{V_1 + V_2} \right) P_2 \tag{A-19}$$

If we define:

$$y_1 = \frac{V_1}{V_1 + V_2} \quad \text{and} \quad y_2 = \frac{V_2}{V_1 + V_2} \tag{A-20}$$

then,

$$P_e = y_1 P_1 + y_2 P_2 \quad \text{or} \quad P_e = y_1 P_1^o + y_2 P_2^o \tag{A-21}$$

with $y_1 + y_2 = 1$. This equation can be used to predict the equilibrium pressure from given system volumes. Conversely, if the equilibrium pressure is evaluated from data, then we can evaluate y_1 and y_2:

$$y_1 = \frac{P_e - P_2^o}{P_1^o - P_2^o} \quad y_2 = \frac{P_1^o - P_e}{P_1^o - P_2^o} \tag{A-22}$$

As P_e, y_1, and y_2 are constants, they can be used to provide a simple way of expressing P_1 and P_2 in terms of each other:

$$P_1 = \left(\frac{1}{y_1} \right) P_e - \left(\frac{y_2}{y_1} \right) P_2 \tag{A-23}$$

$$P_2 = \left(\frac{1}{y_2} \right) P_e - \left(\frac{y_1}{y_2} \right) P_1 \tag{A-24}$$

Finally, if we consider Eq. A-15 on a differential basis, we can relate the time rate change of pressure in both chambers by:

$$V_1 \frac{\mathrm{d}P_1}{\mathrm{d}t} = -V_2 \frac{\mathrm{d}P_2}{\mathrm{d}t} \tag{A-25}$$

If we assume a positive mass flow G denoting flow from chamber 1 to chamber 2, then

$$V_1 \frac{\mathrm{d}P_1}{\mathrm{d}t} = -GR_mT \quad V_2 \frac{\mathrm{d}P_2}{\mathrm{d}t} = GR_mT \tag{A-26}$$

This relationship avoids the need to explicitly consider chamber thermodynamics (albeit as a natural result of assuming isothermal flow conditions).

A-4. Gas Flow Dynamics

Gas flow is considered pseudo-steady and is driven by the difference in upstream and downstream pressures (P_1 and P_2, respectively). If we treat the flow as isothermal at temperature T, the mass flow is governed by [Eq. 4.57 in Coulson et al. (1996)]:

$$\left(\frac{G}{A}\right)^2 \ln\left(\frac{P_2}{P_1}\right)^2 + \frac{P_2^2 - P_1^2}{R_mT} + \frac{4fL}{d}\left(\frac{G}{A}\right)^2 = 0 \tag{A-27}$$

where A is the flow area and f is the Fanning friction factor. If we define:

$$g = \frac{G}{A} \quad \zeta = \left(\frac{P_2}{P_1}\right)^2 \quad \Gamma = \frac{P_1^2}{R_mTg^2} \quad \Lambda = \frac{4fL}{d} \tag{A-28}$$

then,

$$\Gamma = \frac{\Lambda - \ln\zeta}{1-\zeta} \tag{A-29}$$

Here, the Fanning friction factor f is a function of Reynolds number (Re):

$$\mathrm{Re} = \frac{\rho v d}{\mu} = \frac{Gd}{\mu A} = \frac{gd}{\mu} = \left(\frac{4}{\pi}\right)\frac{G}{\mu d} \quad \text{with} \quad A = \frac{\pi}{4}d^2 \tag{A-30}$$

Choked flow occurs at a critical pressure ratio ζ_c defined by:

$$\left.\frac{\mathrm{d}\Gamma}{\mathrm{d}\zeta}\right|_{\zeta=\zeta_c} = 0 \tag{A-31}$$

Application of this criterion to Eq. A-29 leads to:

$$\frac{1}{\zeta_c} = \frac{\Lambda_c - \ln\zeta_c}{1-\zeta_c} \tag{A-32}$$

A-5. Friction Limited Flow

If we assume that flow is dominated by friction such that $\Lambda \gg -\ln\zeta$, then

$$\Gamma \simeq \frac{\Lambda}{1-\zeta} \tag{A-33}$$

Choked flow occurs when:

$$\zeta_c \simeq \frac{1}{1+\Lambda_c} \tag{A-34}$$

Based on ORNL data for Rod 3A1F05 reported in Montgomery and Morris (2019), we use $L \simeq 4\,\mathrm{m}$, $d \simeq 100\,\mu\mathrm{m}$ (from visual inspection), and $f = 0.01$ (assumed), we estimate that:

$$\Lambda_c \simeq \frac{4\,(0.01)\,(4\,\mathrm{m})}{0.0001} = 1600$$

which renders $\zeta_c \simeq 6.3 \times 10^{-4}$. For PNNL evaluations, the maximum upstream pressure $P_1^o = 750\,\mathrm{psi}$ and typical downstream pressure $P_2^o = 14.5\,\mathrm{psi}$ lead to $\zeta \geq 3.7 \times 10^{-4}$. PNNL rods are about four times shorter than ORNL rods, leading to $\Lambda_c \simeq 400$ and $\zeta_c = 2.5 \times 10^{-3}$ under similar crack geometries. As such, it is likely that a portion of the analysis will fall in the choked flow regime. That is, friction will not render the flow un-choked at the initial pressure differentials tested in the current PNNL analysis. Assuming a fixed downstream pressure $P_2 = 14.5\,\mathrm{psi}$, the first upstream pressure below which flow is no longer choked is $P_1 \simeq 300\,\mathrm{psi}$.

From the scaling relationships defined in Eq. A-28, the mass flow per unit area g is related to Γ through:

$$g^2 = \left(\frac{G}{A}\right)^2 = \frac{P_1^2}{\Gamma R_m T} \tag{A-35}$$

In the case of friction limited flow, Eq. A-35 becomes:

$$\left(\frac{4fL}{d}\right) g^2 = \frac{P_1^2 - P_2^2}{R_m T} \tag{A-36}$$

And for laminar flow:

$$f = \frac{16}{\mathrm{Re}} = \frac{16\,\mu}{gd} \tag{A-37}$$

Then,

$$\left(\frac{64\mu L}{d^2}\right) g = \frac{P_1^2 - P_2^2}{R_m T} \tag{A-38}$$

$$\frac{G}{A} = \left(\frac{d^2}{64\mu L R_m T}\right)\left(P_1^2 - P_2^2\right) \tag{A-39}$$

$$G R_m T = \left(\frac{\pi d^4}{256\mu L}\right)\left(P_1^2 - P_2^2\right) \tag{A-40}$$

We let:

$$k = \frac{\pi d^4}{256\mu L} \tag{A-41}$$

Such that:

$$G R_m T = k\left(P_1^2 - P_2^2\right) \tag{A-42}$$

This result, when combined with he rate of pressure change in chamber 1 given by Eq. A-26, yields:

$$V_1 \frac{\mathrm{d}P_1}{\mathrm{d}t} = -k\left(P_1^2 - P_2^2\right) \tag{A-43}$$

From the chamber relationship Eq. A-24, we can write P_2^2 as:

$$P_2^2 = \left[\left(\frac{1}{y_2}\right) P_e - \left(\frac{y_1}{y_2}\right) P_1\right]^2 \tag{A-44}$$

$$= \left(\frac{1}{y_2}\right)^2 P_e^2 - 2\left(\frac{y_1}{y_2^2}\right) P_e P_1 + \left(\frac{y_1}{y_2}\right)^2 P_1^2 \tag{A-45}$$

Then,

$$\frac{\mathrm{d}P_1}{\mathrm{d}t} = -\left(\frac{k}{V_1}\right)\left\{\left[1-\left(\frac{y_1}{y_2}\right)^2\right]P_1^2 + 2\left(\frac{y_1}{y_2^2}\right)P_eP_1 - \left(\frac{1}{y_2}\right)^2 P_e^2\right\} \tag{A-46}$$

$$= -\left(\frac{k}{y_2^2V_1}\right)\left[\left(y_2^2-y_1^2\right)P_1^2 + 2y_1P_eP_1 - P_e^2\right] \tag{A-47}$$

$$= -\left(\frac{k}{y_2^2V_1}\right)\left[\left(y_2-y_1\right)\left(y_2+y_1\right)P_1^2 + 2y_1P_eP_1 - P_e^2\right] \tag{A-48}$$

$$= -\left(\frac{k}{y_1y_2^2V}\right)\left[\left(y_2-y_1\right)P_1^2 + 2y_1P_eP_1 - P_e^2\right] \tag{A-49}$$

$$= \left(\frac{k}{y_1y_2V}\right)\left[\frac{1}{y_2}P_e^2 - 2\left(\frac{y_1}{y_2}\right)P_eP_1 - \left(1-\frac{y_1}{y_2}\right)P_1^2\right] \tag{A-50}$$

$$= \left(\frac{k}{y_1y_2V}\right)\left[\left(\frac{y_1+y_2}{y_2}\right)P_e^2 - 2\left(\frac{y_1}{y_2}\right)P_eP_1 + \left(\frac{y_1}{y_2}-1\right)P_1^2\right] \tag{A-51}$$

$$= \left(\frac{k}{y_1y_2V}\right)\left[\left(\frac{y_1}{y_2}+1\right)P_e^2 - 2\left(\frac{y_1}{y_2}\right)P_eP_1 + \left(\frac{y_1}{y_2}-1\right)P_1^2\right] \tag{A-52}$$

Now let,

$$\mathcal{K} = \frac{k}{y_1y_2V} \quad \alpha = \frac{y_1}{y_2} \tag{A-53}$$

Then,

$$\frac{\mathrm{d}P_1}{\mathrm{d}t} = \mathcal{K}\left[(\alpha+1)P_e^2 - 2\alpha P_eP_1 + (\alpha-1)P_1^2\right] \tag{A-54}$$

We define the pressure and time linearizations such that:

$$P_1 = a + b\phi_1 \quad t = t_o\tau \tag{A-55}$$

where ϕ_1 and τ are the scaled chamber 1 pressure and time, respectively, and a, b, and t_o are arbitrary constants to be later refined to provide the best scaling. Then,

$$\frac{\mathrm{d}P_1}{\mathrm{d}t} = \left(\frac{b}{t_o}\right)\frac{\mathrm{d}\phi_1}{\mathrm{d}\tau} \tag{A-56}$$

$$2\alpha P_eP_1 = 2\alpha P_ea + 2\alpha P_eb\phi_1 \tag{A-57}$$

$$P_1^2 = a^2 + 2ab\phi_1 + b^2\phi_1^2 \tag{A-58}$$

Using this expression for the squre of P_1, we can evaluate the right-hand quadratic pressure grouping in Eq. refeq:simform. It is:

$$(\alpha+1)P_e^2 - 2\alpha P_eP_1 + (\alpha-1)P_1^2 \tag{A-59}$$

$$(\alpha+1)P_e^2 - 2\alpha P_ea - 2\alpha P_eb\phi_1 + (\alpha-1)\left(a^2 + 2ab\phi_1 + b^2\phi_1^2\right) \tag{A-60}$$

$$\left[(\alpha+1)P_e^2 - 2\alpha P_ea + (\alpha-1)a^2\right] + \left[-2\alpha P_eb + 2(\alpha-1)ab\right]\phi_1 + \left[(\alpha-1)b^2\right]\phi_1^2 \tag{A-61}$$

If we seek a such that the group of order ϕ_1 becomes zero, then:

$$-2\alpha P_eb + 2(\alpha-1)ab = 0 \tag{A-62}$$

$$\left[-\alpha P_e + (\alpha-1)a\right]b = 0 \tag{A-63}$$

$$-\alpha P_e + (\alpha-1)a = 0 \tag{A-64}$$

$$a = \left(\frac{\alpha}{\alpha-1}\right)P_e \tag{A-65}$$

Then the zeroth order ϕ_1 term becomes:

$$(\alpha+1)\,P_e^2 - 2\alpha P_e a + (\alpha-1)\,a^2 \tag{A-66}$$

$$(\alpha+1)\,P_e^2 - 2\left(\frac{\alpha^2}{\alpha-1}\right)P_e^2 + (\alpha-1)\left[\frac{\alpha^2}{(\alpha-1)^2}\right]P_e^2 \tag{A-67}$$

$$(\alpha+1)\,P_e^2 - 2\left(\frac{\alpha^2}{\alpha-1}\right)P_e^2 + \left(\frac{\alpha^2}{\alpha-1}\right)P_e^2 \tag{A-68}$$

$$\left[\alpha+1-\frac{\alpha^2}{\alpha-1}\right]P_e^2 \tag{A-69}$$

$$\left[\frac{(\alpha+1)(\alpha-1)-\alpha^2}{\alpha-1}\right]P_e^2 \tag{A-70}$$

$$\left(\frac{\alpha^2-1-\alpha^2}{\alpha-1}\right)P_e^2 \tag{A-71}$$

$$-\left(\frac{1}{\alpha-1}\right)P_e^2 \tag{A-72}$$

To reduce the problem further, we seek a second-order ϕ_1 coefficient equal -1 such that the scaled denominator forms $1-\phi_1^2$. To do this, the second order coefficient must be:

$$(\alpha-1)\,b^2 = \left(\frac{1}{\alpha-1}\right)P_e^2 \tag{A-73}$$

$$b^2 = \left[\frac{1}{(\alpha-1)^2}\right]P_e^2 \tag{A-74}$$

$$b = \pm\left(\frac{1}{\alpha-1}\right)P_e \tag{A-75}$$

We take the negative root. Thus,

$$a = -\alpha b \quad b = -\left(\frac{1}{\alpha-1}\right)P_e \tag{A-76}$$

So the final scaled form of Eq. A-55 becomes:

$$P_1 = a + b\phi_1 \tag{A-77}$$

$$= b\,(\phi_1-\alpha) \tag{A-78}$$

$$= -\left(\frac{\phi_1-\alpha}{\alpha-1}\right)P_e \tag{A-79}$$

Entering this expression in our original polynomial,

$$(\alpha-1)\,P_1^2 = (\phi_1-\alpha)^2\left(\frac{P_e^2}{\alpha-1}\right) \tag{A-80}$$

$$= \left(\phi_1^2 - 2\alpha\phi + \alpha^2\right)\left(\frac{P_e^2}{\alpha-1}\right) \tag{A-81}$$

$$2\alpha P_e P_1 = -2\alpha\,(\phi-\alpha)\left(\frac{P_e^2}{\alpha-1}\right) \tag{A-82}$$

$$= \left(-2\alpha\phi + 2\alpha^2\right)\left(\frac{P_e^2}{\alpha-1}\right) \tag{A-83}$$

$$(\alpha+1)\,P_e^2 = \left[(\alpha+1)(\alpha-1)\right]\left(\frac{P_e^2}{\alpha-1}\right) \tag{A-84}$$

$$= \left(\alpha^2-1\right)\left(\frac{P_e^2}{\alpha-1}\right) \tag{A-85}$$

The above suggests

$$(\alpha+1)\,P_e^2 - 2\alpha P_e P_1 + (\alpha-1)\,P_1^2 \tag{A-86}$$

$$\left[\alpha^2 - 1 + 2\alpha\phi - 2\alpha^2 + \phi_1^2 - 2\alpha\phi + \alpha^2\right]\left(\frac{P_e^2}{\alpha-1}\right) \tag{A-87}$$

$$\left(\phi_1^2 - 1\right)\left(\frac{P_e^2}{\alpha-1}\right) \tag{A-88}$$

$$-\left(1-\phi_1^2\right)\left(\frac{P_e^2}{\alpha-1}\right) \tag{A-89}$$

$$bP_e\left(1-\phi_1^2\right) \tag{A-90}$$

Now, returning to our original differential equation [Eq. A-54],

$$\frac{\mathrm{d}P_1}{\mathrm{d}t} = \mathcal{K}\left[(\alpha+1)\,P_e^2 - 2\alpha P_e P_1 + (\alpha-1)\,P_1^2\right] \tag{A-91}$$

$$\left(\frac{b}{t_o}\right)\frac{\mathrm{d}\phi_1}{\mathrm{d}\tau} = \mathcal{K}bP_e\left(1-\phi_1^2\right) \tag{A-92}$$

$$\frac{\mathrm{d}\phi_1}{\mathrm{d}\tau} = \mathcal{K}P_e t_o\left(1-\phi_1^2\right) \tag{A-93}$$

If we define:

$$t_o = \frac{1}{2\mathcal{K}P_e} \tag{A-94}$$

then the differential equation becomes:

$$\frac{\mathrm{d}\phi_1}{\mathrm{d}\tau} = \frac{1}{2}\left(1-\phi_1^2\right) \tag{A-95}$$

This has the solution

$$\phi_1 = \frac{e^\tau - \theta_1}{e^\tau + \theta_1} \tag{A-96}$$

with

$$\theta_1 = \frac{1-\phi_1^o}{1+\phi_1^o} \tag{A-97}$$

Now,

$$\begin{aligned}\phi_1 &= \frac{P_1 - a}{b} && \text{(A-98)}\\ &= \frac{P_1}{b} + \alpha && \text{(A-99)}\\ &= \alpha + (1-\alpha)\left(\frac{P_1}{P_e}\right) && \text{(A-100)}\end{aligned}$$

Thus,

$$\phi_1^o = \alpha + (1-\alpha)\left(\frac{P_1^o}{P_e}\right) \tag{A-101}$$

Now for chamber 2, we can use Eq. A-23 to write:

$$P_1^2 = \left(\frac{1}{y_1}\right)^2 P_e^2 - 2\left(\frac{y_2}{y_1^2}\right)P_eP_2 + \left(\frac{y_2}{y_1}\right)^2 P_2^2 \tag{A-102}$$

Then,

$$V_2 \frac{\mathrm{d}P_2}{\mathrm{d}t} = G R_m T \tag{A-103}$$

$$V_2 \frac{\mathrm{d}P_2}{\mathrm{d}t} = k\left(P_1^2 - P_2^2\right) \tag{A-104}$$

$$\frac{\mathrm{d}P_2}{\mathrm{d}t} = -\left(\frac{k}{y_2 V}\right)\left(P_2^2 - P_1^2\right) \tag{A-105}$$

$$\frac{\mathrm{d}P_2}{\mathrm{d}t} = -\left(\frac{k}{y_2 V}\right)\left\{\left[1 - \left(\frac{y_2}{y_1}\right)^2\right] P_2^2 + 2\left(\frac{y_2}{y_1^2}\right) P_e P_2 - \left(\frac{1}{y_1}\right)^2 P_e^2\right\} \tag{A-106}$$

$$\frac{\mathrm{d}P_2}{\mathrm{d}t} = -\left(\frac{k}{y_1^2 y_2 V}\right)\left[\left(y_1^2 - y_2^2\right) P_2^2 + 2 y_2 P_e P_2 - P_e^2\right] \tag{A-107}$$

$$\frac{\mathrm{d}P_2}{\mathrm{d}t} = -\left(\frac{k}{y_1^2 y_2 V}\right)\left[\left(y_1 - y_2\right) P_2^2 + 2 y_2 P_e P_2 - P_e^2\right] \tag{A-108}$$

$$\frac{\mathrm{d}P_2}{\mathrm{d}t} = \left(\frac{k}{y_1 y_2 V}\right)\left[\left(\frac{1}{y_1}\right) P_e^2 - 2\left(\frac{y_2}{y_1}\right) P_e P_2 - \left(1 - \frac{y_2}{y_1}\right) P_2^2\right] \tag{A-109}$$

$$\frac{\mathrm{d}P_2}{\mathrm{d}t} = \left(\frac{k}{y_1 y_2 V}\right)\left[\left(\frac{y_1 + y_2}{y_1}\right) P_e^2 - 2\left(\frac{y_2}{y_1}\right) P_e P_2 + \left(\frac{y_2}{y_1} + 1\right) P_2^2\right] \tag{A-110}$$

$$\frac{\mathrm{d}P_2}{\mathrm{d}t} = \left(\frac{k}{y_1 y_2 V}\right)\left[\left(\frac{y_2}{y_1} + 1\right) P_e^2 - 2\left(\frac{y_2}{y_1}\right) P_e P_2 + \left(\frac{y_2}{y_1} + 1\right) P_2^2\right] \tag{A-111}$$

And we let,

$$\beta = \frac{1}{\alpha} = \frac{y_2}{y_1} \tag{A-112}$$

Then,

$$\frac{\mathrm{d}P_2}{\mathrm{d}t} = \mathcal{K}\left[\left(\beta + 1\right) P_e^2 - 2\beta P_e P_2 + \left(\beta + 1\right) P_2^2\right] \tag{A-113}$$

This expression is analogous to Eq. A-54. If we let:

$$t = t_o \tau \quad P_2 = a' + b' \phi_2 \tag{A-114}$$

where t_o', a', and b' are arbitrary constants used to reduce the differential equation to a simpler form, then Eq. A-113 reduces to

$$\frac{\mathrm{d}\phi_2}{\mathrm{d}\tau} = \frac{1}{2}\left(1 - \phi_2^2\right) \tag{A-115}$$

when

$$t_o' = \frac{1}{2\mathcal{K} P_e} \quad a' = \beta b' \quad b' = -\left(\frac{1}{\beta - 1}\right) P_e \tag{A-116}$$

So, Eq. A-115 has the solution

$$\phi_2 = \frac{e^\tau - \theta_2}{e^\tau + \theta_2} \tag{A-117}$$

with

$$\theta_2 = \frac{1 - \phi_2^o}{1 + \phi_2^o} \tag{A-118}$$

In this case, the time-scaling is identical to chamber 1. Then,

$$\phi_2 = \beta + (1 - \beta)\left(\frac{P_2}{P_e}\right) \tag{A-119}$$

$$= \frac{1}{\alpha} + \left(1 - \frac{1}{\alpha}\right)\left(\frac{P_2}{P_e}\right) \tag{A-120}$$

Such that

$$\phi_2^o = \beta + (1-\beta)\left(\frac{P_2^o}{P_e}\right) \tag{A-121}$$

We seek to relate ϕ_1 and ϕ_2. Starting with the chamber equilibrium pressure relationship (Eq. A-21):

$$y_1 P_1 + y_2 P_2 = P_e \tag{A-122}$$

$$y_1\left(\frac{P_1}{P_e}\right) + y_2\left(\frac{P_2}{P_e}\right) = 1 \tag{A-123}$$

$$\left(\frac{y_1}{y_2}\right)\left(\frac{P_1}{P_e}\right) + \left(\frac{P_2}{P_e}\right) = \frac{y_1+y_2}{y_2} \tag{A-124}$$

$$\alpha\left(\frac{P_1}{P_e}\right) + \left(\frac{P_2}{P_e}\right) = \alpha + 1 \tag{A-125}$$

Eq. A-79 for P_1 and a similar equation for P_2 can be used to write:

$$\frac{P_1}{P_e} = \frac{\phi_1-\alpha}{1-\alpha} \quad \frac{P_2}{P_e} = \frac{\phi_2-\beta}{1-\beta} \tag{A-126}$$

Then,

$$\alpha\left(\frac{\phi_1-\alpha}{1-\alpha}\right) + \left(\frac{\phi_2-\beta}{1-\beta}\right) = \alpha+1 \tag{A-127}$$

$$\alpha\phi_1 - \alpha^2 + (1-\alpha)\left(\frac{\phi_2-\beta}{1-\beta}\right) = (1+\alpha)(1-\alpha) \tag{A-128}$$

$$\alpha\phi_1 - \alpha^2 + (1-\alpha)\left(\frac{\phi_2-\beta}{1-\beta}\right) = 1-\alpha^2 \tag{A-129}$$

$$\alpha\phi_1 + (1-\alpha)\left(\frac{\phi_2-\beta}{1-\beta}\right) = 1 \tag{A-130}$$

$$\alpha(1-\beta)\phi_1 + (1-\alpha)(\phi_2-\beta) = 1-\beta \tag{A-131}$$

$$(\alpha-\alpha\beta)\phi_1 + \phi_2 - \beta - \alpha(\phi_2-\beta) = 1-\beta \tag{A-132}$$

$$(\alpha-\alpha\beta)\phi_1 + \phi_2 - (\alpha\phi_2-\alpha\beta) = 1 \tag{A-133}$$

Now, we know $\alpha\beta = 1$, such that:

$$(\alpha-1)\phi_1 + \phi_2 - (\alpha\phi_2 - 1) = 1 \tag{A-134}$$

$$(\alpha-1)\phi_1 + \phi_2 - \alpha\phi_2 + 1 = 1 \tag{A-135}$$

$$(\alpha-1)\phi_1 - (\alpha-1)\phi_2 = 0 \tag{A-136}$$

$$(\alpha-1)\phi_1 = (\alpha-1)\phi_2 \tag{A-137}$$

$$\phi_1 = \phi_2 \tag{A-138}$$

So the coordinate transformations render ϕ_1 and ϕ_2 identical. This means that ϕ_1^o and ϕ_2^o are identical, and similarly, that θ_1 and θ_2 are identical.

A-6. Decay to Atmospheric

At the end of each test, the downstream is vented and the upstream is then allowed to decay to atmospheric. We evaluate this in the laminar un-choked flow regime below.

For laminar un-choked flow, the basic equations for gas flow remain unchanged, save for the fact that P_2 is now fixed at its initial value P_2^o, which corresponds to atmospheric pressure. We have:

$$V_1\frac{\mathrm{d}P_1}{\mathrm{d}t} = -k\left[P_1^2 - \left(P_2^o\right)^2\right] \tag{A-139}$$

We define our scaling factors as:

$$t = t_o \tau \quad P_1 = a + b\phi \tag{A-140}$$

Then,

$$\left(\frac{V_1 b}{t_o}\right)\frac{\mathrm{d}\phi}{\mathrm{d}\tau} = -k\left[b^2\phi^2 + ab\phi + a^2 - \left(P_2^o\right)^2\right] \tag{A-141}$$

If we let $a = 0$ and $b = P_2^o$, then

$$\frac{\mathrm{d}\phi}{\mathrm{d}\tau} = -\left(\frac{kt_o}{V_1 b}\right)\left[b^2\phi^2 + -b^2\right] \tag{A-142}$$

$$= \left(\frac{kP_2^o t_o}{V_1}\right)\left(1 - \phi^2\right) \tag{A-143}$$

Finally, we set:

$$t_o = \frac{y_1 V}{2kP_2^o} \tag{A-144}$$

so that we regain:

$$\frac{\mathrm{d}\phi}{\mathrm{d}\tau} = \frac{1}{2}\left(1 - \phi^2\right) \tag{A-145}$$

with

$$\phi = \frac{P_1}{P_2^o} \quad t_o = \frac{y_1 V}{2kP_2^o} \tag{A-146}$$

The solution is again:

$$\phi = \frac{e^\tau - \theta}{e^\tau + \theta} \tag{A-147}$$

with

$$\theta = \frac{1 - \phi^o}{1 + \phi^o} \quad \phi_o = \frac{P_1^o}{P_2^o} \tag{A-148}$$

A-7. Permeability

Resistance to flow is often expressed in terms of permeability K (not to be confused with the grouped constant $\mathcal{K}$). The permeability K derives from Darcy's equation for flow of incompressible fluids in porous media is defined by Dallavalle (1948) as:

$$K = \frac{\mu q L}{A\left(P_1 - P_2\right)} \tag{A-149}$$

where q is volumetric flow rate. The permeability associated with flow through a pipe or capillary of diameter d can be defined by substitution Poisueille's Law for incompressible flow in Eq. A-149. Poisueille's Law is (Dallavalle, 1948):

$$q = \left(\frac{\pi d^4}{128\mu}\right)\left(\frac{P_1 - P_2}{L}\right) \tag{A-150}$$

If we take the flow area as the true area of the capillary, then $A = \pi d^2/4$ and,

$$K = \frac{d^2}{32} \tag{A-151}$$

Starting with Eq. A-40, we can write:

$$GR_m T = \left(\frac{\pi d^4}{256\mu L}\right)\left(P_1^2 - P_2^2\right) \tag{A-152}$$

$$GR_m T = \left(\frac{KA}{2\mu L}\right)\left(P_1^2 - P_2^2\right) \tag{A-153}$$

While the current analysis treats the flow path as an ideal capillary or pipeline of singular known diameter d, the hydraulic path in tortuous media such as spent nuclear fuel is not fixed (and can vary along the length of the path) and is not known. As discussed in the main body, this does not prevent interpreting flow by assuming a single effective hydraulic diameter. However, as done in Montgomery and Morris (2019), flow through spent fuel is typically characterized by permeability based on the cross-sectional area A_x of the fuel rod (which is orders of magnitude larger than the effective hydraulic diameter of the fuel itself). The derivation herein assumes an area A based on the hydraulic diameter, and it follows that the permeability K based on this area will differ from a permeability based on the cross-sectional area A_x. To distinguish between the two measures of permeability, we shall call K the unnormalized permeability and define a new permeability K_n (termed the normalized permeability) based on A_x. If laminar un-choked mass flow is treated using the normalized permeability, then Eq. A-153 becomes:

$$GR_mT = \left(\frac{K_nA_x}{2\mu L}\right)\left(P_1^2 - P_2^2\right) \tag{A-154}$$

By comparison of Eqs. A-153 and A-154, we can write:

$$K_nA_x = KA \tag{A-155}$$

$$K_n = \left(\frac{A}{A_x}\right)K \tag{A-156}$$

Assuming the media is relatively uniform along the length of the hydraulic path, we can relate the ratio of flow channel area A to total cross-sectional area A_x to the void fraction ϵ of the media. The void fraction is defined as the void volume V_v to the total volume of the rod V

$$\epsilon = \frac{V_v}{V} \simeq \frac{AL}{A_xL} = \frac{A}{A_x} \tag{A-157}$$

Thus,

$$K_n = \epsilon K \tag{A-158}$$

As $\epsilon < 1$, $K_n < K$.

Appendix A References

Coulson JM, JF Richardson, JR Backhurst, and JH Harker. 1996. *Chemical Engineering: Fluid Flow, Heat Transfer and Mass Transfer*, fifth edition, Vol. 1. Butterworth-Heinemann Ltd., Oxford.

Dallavalle JM. 1948. *Micromeritics: the Technology of Fine Particles*, second edition. Pitman Publishing Corporation, New York.

Montgomery R and RN Morris. 2019. “Measurement and modeling of the gas permeability of high burnup pressurized water reactor fuel rods.” *Journal of Nuclear Materials* 523:206–215.